LARGE ANGLE BEAMSTRAHLUNG DETECTOR FOR LUMINOSITY MONITORING AND OPTIMIZATION AT CESR

by

ERIC E. WISNIEWSKI

THESIS

Submitted to the Graduate School

of Wayne State University

in partial fulfillment of the requirements

for the degree of

MASTER OF SCIENCE

2008

MAJOR: Physics

Approved by:

Advisor Date

Contents

List of Figures

List of Tables

Chapter 1

CESR and the Importance of Luminosity

1.1 Description of CESR

The Cornell Electron-positron Storage Ring (CESR), is an electron-positron collider located on the Cornell University campus, in Ithaca, New York and operated by the Laboratory for Elementary Particle Physics (LEPP). It is used alternately for high energy physics (HEP) experiments (as a charm-tau factory employing the CLEO detector) and as a first generation synchrotron light source (CHESS). Our large angle beamstrahlung detector experiments are focussed entirely on the HEP type lattices and configurations (colliding beams are required for beamstrahlung).

1.1.1 CESR Components and Operation

The major components of CESR include a linear accelerator (LINAC), synchrotron, and the storage ring. The LINAC first produces electrons and positrons by means of an electron gun with a tungsten target electron-positron converter. Then these particles are pre-bunched and accelerated by radio frequency (RF) cavities – the electrons to an energy of about 300

MeV and positrons to an energy of about 150-200 MeV. Then, for further acceleration, they enter the synchrotron which circulates the particles in a magnetic guide field through an evacuated beam pipe. Here the particle energy is increased to the required level (about 2 GeV under CESR-c HEP conditions) by means of RF cavities operating at 500 MHz. From the synchrotron the bunched particles are injected into the storage ring, which has its own high precision magnetic guide field or "lattice" and an even higher quality vacuum both of which are required to allow the beams to coast for hours. The particles are injected into the storage ring following a carefully controlled bunch pattern consisting of up to 9 trains of up to 5 bunches yielding a maximum total of 45 bunches each of e- and e+, counter-rotating, with positrons traveling clockwise and electrons traveling counter-clockwise (see Figure 1.1). The counter-rotating bunched beams are separated electrostatically to avoid unwanted collisions and wasted luminosity following a so-called "pretzel scheme" which was invented and developed at CESR, as shown in Figure 1.2. The beams collide at the single Interaction Point (IP), which is located inside the CLEO detector. For CESR-c, the trains are spaced either 75.6m or 79.8 m apart and within the trains bunches are spaced 4.2 m apart [3]. Superconducting radio frequency (SRF) cavities operating at 500 MHz are required to keep the bunches circulating, replacing the energy lost to synchrotron radiation. Superconducting quadrupole magnets near the IP contained within a solenoidal field provide the final focus, squeezing the beams to the smallest size possible to provide maximum luminosity.

1.1.2 Evolution of CESR

CESR was built to store beams produced by the existing Cornell synchrotron and began operations in 1979. The storage ring was originally designed for High Energy Physics experiments with energies in the 4.5-6 GeV/beam range. CHESS was constructed from 1978-1980 and operated parasitically, switching to alternate running when CESR energies dropped too low (less than 5 GeV/beam). CESR has been operating successfully at lower energies since 2004, after the upgrade which included the installation of 12 wigglers to pro-

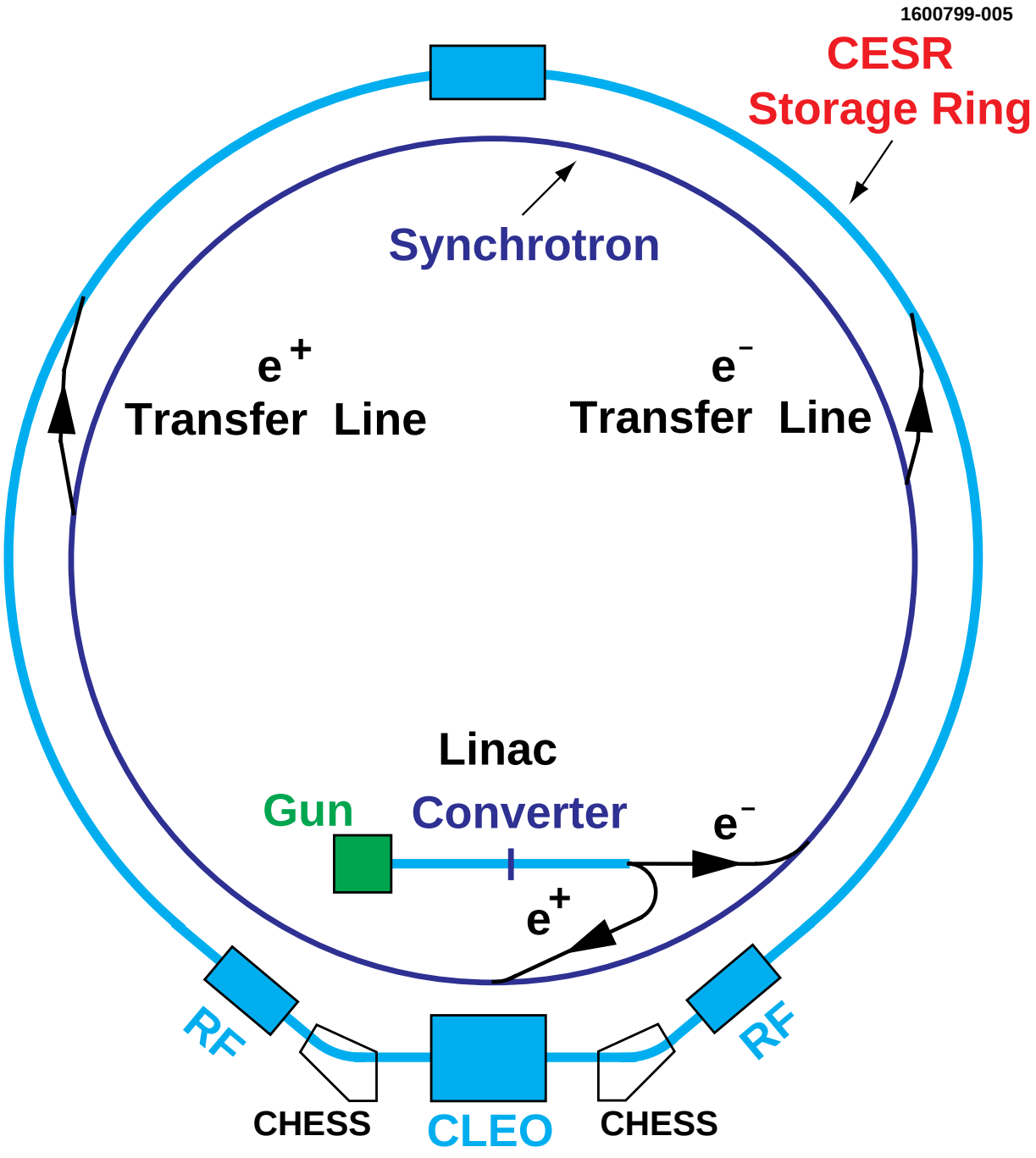

Figure 1.1: Schematic: Cornell Electron-positron Storage Ring (CESR)

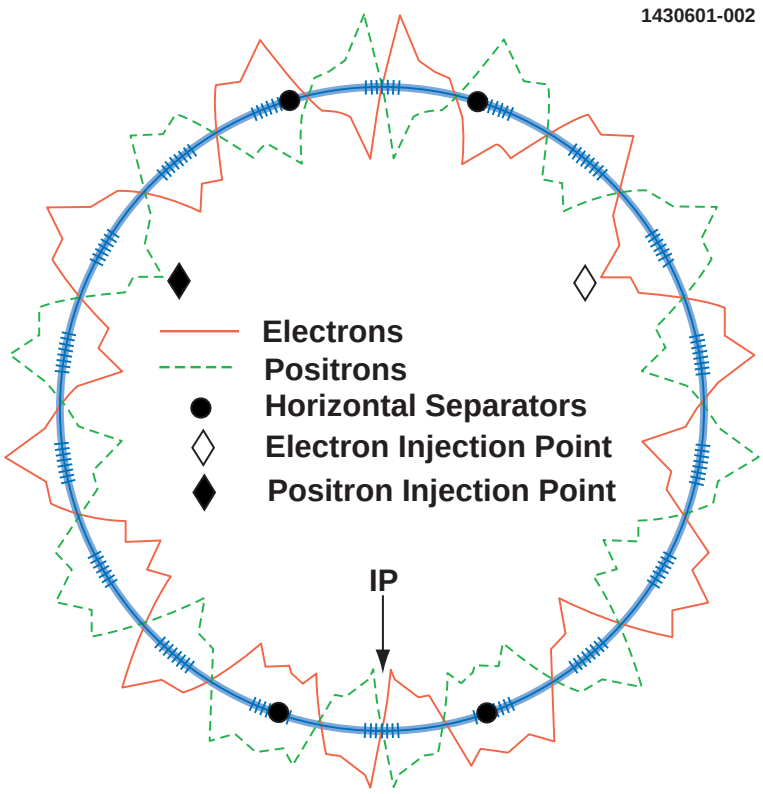

Figure 1.2: An illustration of the pretzel scheme used at CESR. In order to avoid unwanted luminosity-wasting collisions, the beams are separated electrostatically at all crossing points except at the Interaction Point (IP) inside the CLEO detector.

vide adequate radiation damping[6]. In its present incarnation, CESR-c, energies lie in the 1.8 - 2.5 GeV/beam range. Table 1.1 presents some typical CESR-c operating parameters in 2007, compared to the higher energy CESR Phase III of the period mid 1990s-2002.

	CESR(mid 1990s)	CESR(ca.2000)	CESR-c 2007
Energy (GeV/beam)	5.3	5.3	2.1
Circumference (m)	768	768	768
Avg. beam current/species (mA)	120	340	62
No. of Bunches	18	45	24
Bunch pattern	9 trains of 2	9 trains of 5	8 trains of 3
σ_x (μm)	500	460	340
σ_y (μm)	11	4	5.7
σ_z (mm)	18	18	10.7
Crossing Angle (mrad)	$\pm$2.0	$\pm$2.0	$\pm$3.0
Luminosity (10^{30}cm^{-2}s^{-1})	330	1280	60

Table 1.1: A Comparison of some "typical" CESR and CESR-c (charm-tau factory) parameters. The values listed here are reflective of conditions for the time periods listed at the top of the table, during which other values may also apply. Most of these parameters are dynamic and will vary during the course of a run [3],[4],[5].

1.2 CESR Luminosity and Large Angle Beamstrahlung

1.2.1 Luminosity Definition

In serving its function as an HEP machine, the primary concern at CESR is to maximize luminosity in order to provide copious events for particle physicists to observe using the CLEO detector. Luminosity for a single collision is defined as "the number of reaction events produced per unit reaction cross-section" [7] due to the overlap of the density functions of two colliding beams in space-time. Thus, the luminosity for a single beam crossing, L_{sc}, is given by the overlap integral[7]:

$$L_{sc} = \frac{1}{c}\int dV d\tau \rho_1(\mathbf{r},\tau)\rho_2(\mathbf{r},\tau) \times c\sqrt{(\mathbf{v_1}-\mathbf{v_2})^2 - (\mathbf{v_1}\times\mathbf{v_2})^2} \tag{1.1}$$

where dV is the volume element, $\rho_{1(2)}$ are the normalized density functions for the two beams, $\mathbf{v_{1(2)}}$ are the common velocities in the lab frame of the particles in each of the two bunches, c is the speed of light in vacuum and τ is the time. Equation 1.1 is relativistically invariant. For the case of relativistic beams colliding head-on, a simplifying approximation yields this equation [8]:

$$L_{sc} = 2c \int dV d\tau \rho_1(\mathbf{r}, \tau) \rho_2(\mathbf{r}, \tau) \tag{1.2}$$

1.2.2 Optimal Luminosity

The equation for optimal luminosity (L_0) derived from Eq. 1.2 in the case of two Gaussian beams of the same size and aspect ratio, containing the same amount of charge, both traveling at the speed of light and colliding with perfect alignment is[9],[10]:

$$L_0 = 2c \frac{N_1 N_2}{(2\pi)^3 \sigma_x \sigma_y \sigma_z} \int dV d\tau e^{-(x^2/\sigma_x^2 + y^2/\sigma_y^2 + (z^2 + (c\tau)^2)/\sigma_z^2)} \tag{1.3}$$

$$= \frac{f_c N_1 N_2}{4\pi \sigma_x \sigma_y} \tag{1.4}$$

with $N_{1(2)}$ the number of particles in each beam, and σ_x, σ_y and σ_z are the beam dimensions. f_c is the collision frequency, dV is the volume element, c is the speed of light in vacuum and τ is the time.

1.2.3 Limits on Luminosity and Beam-Beam Effects

From Eq. 1.4 it appears that achieving increased luminosity is a matter of making the beams' transverse cross-sections smaller and/or increasing the number of charged particles in each bunch, thus increasing the density and therefore the luminosity. However, the capacity to do this is limited by the beam-beam interaction. As the charge density is increased, the luminosity increases but so do beam-beam interaction effects.[9]

With increasing luminosity the charge per unit area in each beam becomes so large that the electromagnetic fields felt by one beam due to the other are quite significant, leading

to instabilities which actually decrease luminosity. These beam-beam effects are typically non-linear and quite difficult to characterize.

The basic effect is the same (the particles of one beam are deflected by the field of the other beam) in all accelerators, and so long as the effect is small at least one consequence is beneficial. All particles are focussed towards the center of the other beam, the effective transverse beam sizes decrease, and the luminosity increases.

Circular accelerators (where the large angle beamstrahlung technique is being developed) and linear accelerators (where, presumably, the technique will be most useful) differ in the details of how a too strong beam-beam interaction can affect the machine. In a circular accelerator, where beams are kept for billions of revolution, operators strive to maintain a stable beam. A particle executes a number of transverse (betatron) oscillations around the nominal orbit during a revolution, and that number is called the Q-value of the machine. There are imperfections in the magnetic lattice, which will impart a particle an unwanted transverse kick. If the particle executes exactly an integer number N of oscillations around the ring (Q=N), it will return to the same spot and be kicked again. The kicks will add resonantly, inducing either beam size growth or particle losses, both of which decrease the luminosity. Even if Q=N+1/3, the particle will return to the same spot every three revolutions, still being subject to resonant instabilities.

Thus the need to keep both the vertical and horizontal Q as far away as possible from rational values. The tune shift is the average shift in the oscillation angle, due to the deflection in the beam-beam interaction. The spread in the deflection is equal to the average deflection, effectively pushing some particles close to rational values of Q. The horizontal and vertical tune shifts are

$$\xi_x = \frac{N_{1(2)} r_e \beta^*{}_x}{2\pi\gamma\sigma_x(\sigma_x + \sigma_y)} \tag{1.5}$$

and

$$\xi_y = \frac{N_{1(2)} r_e \beta^*{}_y}{2\pi\gamma\sigma_y(\sigma_x + \sigma_y)} \tag{1.6}$$

where $N_{1(2)}$ is the number of particles in each beam, r_e is the classical electron radius, $\beta^*{}_{y(x)}$ is the betatron amplitude function at the interaction point (IP), γ is the relativistic factor, and the other factors were defined previously. Simulations indicate that storage rings become unstable when the tune shifts exceed 0.06. Smaller values will still increase the beam size, leading to smaller luminosity. CESR-c works with tune shifts below or at 0.04.

Eqs. 1.5 and 1.6 show that there is a fundamental limit to the luminosity of a storage ring. In practice, the only parameters that can be decreased without also decreasing the value of Eq. 1.4 are the β^*. These are limited by how strong a final quadrupole near CLEO can be made, and also how close to the IP it can be placed (too close, it will interfere with the detector).

In a linear accelerator, one is concerned with maintaining particle angles such that, after the collision, the beams are still contained within the beam pipe. This, too, will limit the transverse charge density of the beams, and therefore the luminosity. For a single pass linear collider it is best to consider the disruption parameter, equal to the tune shift except for the $(\beta^* \rightarrow \sigma_z)$ substitution and an overall 4π factor

$$D_x = \frac{2N_{1(2)} r_e \sigma_z}{\gamma\sigma_x(\sigma_x + \sigma_y)} \tag{1.7}$$

and

$$D_y = \frac{2N_{1(2)} r_e \sigma_z}{\gamma\sigma_y(\sigma_x + \sigma_y)}. \tag{1.8}$$

Simulations indicate that the luminosity will increase for higher D, up to about a value of 6, after which the beams disrupt each other so much (see Fig. 1.3 and Ref.[1]) that luminosity is typically decreased.

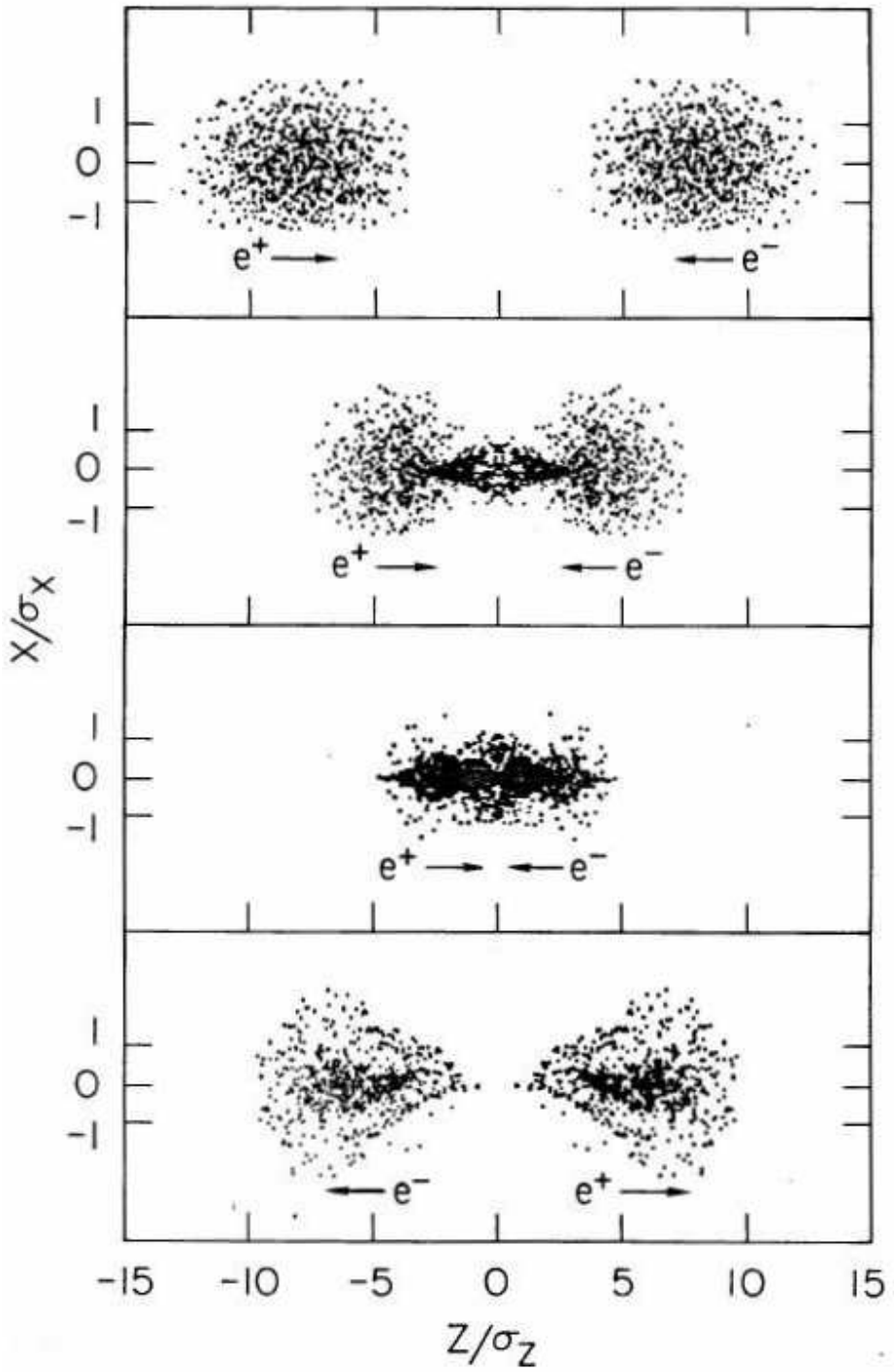

Figure 1.3: A beam-beam effect example. Computer simulated single-pass collision of intense relativistic beams illustrating the pinch effect.[1]

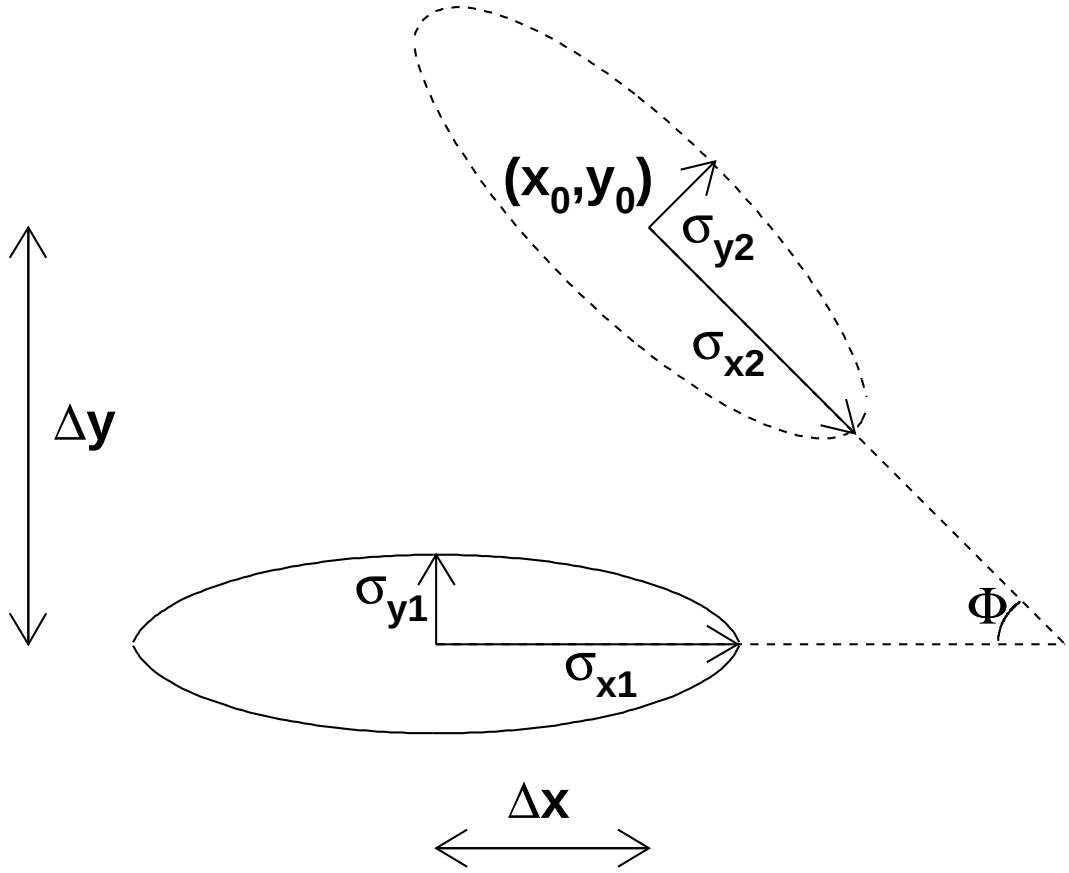

Figure 1.4: Seven degrees of freedom of the general beam-beam collision. Includes two transverse dimensions for each beam, a 2D vector connecting the centroids of the beams (impact parameter), and one relative rotation.[2]

1.2.4 Luminosity at a Linear Collider.

In a circular ring, where no pretzel or other beam separation scheme is implemented, both the electron and positron beams move along the same magnetic waveguide and have therefore the same phase space characteristics, including the same size and trajectory at the IP. The pretzel scheme makes it possible for beams to sample different magnetic fields due to different trajectories, and the beams will typically be slightly different at the CLEO IP.

In a linear collider, however, the beams are accelerated by completely independent accelerators, and can be substantially different. Figure 1.4 provides a cartoon for the transverse degrees of freedom of the two beams, under the assumption that their transverse profile be Gaussian.

This amounts to seven degrees of freedom – three for the alignment in the transverse plane (x, y, and the rotation angle Φ), plus the transverse beam sizes, two for each beam (σ_{x1}, σ_{y1}, σ_{x2}, and σ_{y2} (as shown in Figure 1.4). An additional degree of freedom is introduced if there is a crossing angle, as is the case at CESR. The ideal instrument is one which will continuously and passively monitor the pathology of the beam-beam collision without disturbing the run, allowing for its incorporation into the existing instrumentation as a feedback device. A large angle beamstrahlung detector has been proposed as such a device[2].

Despite the decrease in energy and beam current, CESR should still be a good facility for testing the feasibility of this type of instrument because it has well-known parameters for comparison, parameters well-known by other means. At present a Coherent Beam-Beam Interaction (BBI) luminosity monitor is in place[11], which shakes selected bunches using a lock-in amplifier, and uses feedback from the strength of the BBI for tuning. This is decidedly not a passive device and furthermore will not work at a linear accelerator or other asymmetric machines. As is almost always the case at electron-positron storage rings, the beams are very flat, (at CESR a typical aspect ratio σ_y/σ_x is 0.02[5]) so a primary area of concern is drift in the vertical (y) direction. For instance, if the beams' centroids drift apart in the vertical direction by σ_y, a quantity on the order of a few microns, virtually all luminosity will be lost. As explained in the next section, a large angle beamstrahlung detector is quite sensitive to such a drift in the alignment, as well as to the beam dimensions. The development of this device could prove to be very important to the successful and optimal operation of future linear colliders such as the ILC [12].

Chapter 2

Beamstrahlung

2.1 Overview: Definitions and General Properties

Beamstrahlung is synchrotron radiation emitted by a particle beam when it is deflected by the electromagnetic field of the colliding beam, typically at the interaction point (IP) of a collider or storage ring. The first observation of beamstrahlung was made at Stanford University at the SLC, reported in 1989 [13].

The typical beamstrahlung radiation energy can, at future linear colliders, be of the order of the beam energy, in which case a quantum mechanical treatment is in order. However, at current or future circular accelerators, the soft, large angle radiation of interest here can be treated classically. This is the approach presented here.

The properties of beamstrahlung can, for the most part, be derived via the formulas in Ref. [14], (ie. using the "searchlight" approximation), convoluted over the charge distributions in space-time. From this type of analysis it can be seen that most of the radiation is in the form of hard x-rays emitted in the forward direction within a conical region with opening angle $1/\gamma$, where γ is the relativistic factor.

2.2 Large Angle Beamstrahlung

However, in our case we are interested only in large angle beamstrahlung, emitted at angles much greater than $1/\gamma$ and at much lower energies ie. at wavelengths from visible to infra-red. In this regime the searchlight approximation fails and the "short magnet" approximation is valid[15],[16].

2.3 Properties

2.3.1 Total Beamstrahlung Power Emitted

First we will consider the case of head-on collision of two Gaussian beams of equal size, energy and mass. The total beamstrahlung power emitted by beam 1 (W_1) when it is deflected by the force arising from the fields of the particles of beam 2 is [17]

$$W_1 = f_c U_1 \tag{2.1}$$

$$= g(r) {r_e}^3 mc^2 \gamma^2 \frac{f_c N_1 {N_2}^2}{4\pi\sigma_x\sigma_y\sigma_z} \tag{2.2}$$

$$= g(r) {r_e}^3 mc^2 \gamma^2 \frac{L_0 N_2}{\sigma_z} \tag{2.3}$$

In these equations f_c is the beam collision frequency (the product of the revolution frequency of the ring f_0 and B the number per species of circulating bunches), U_1 is the energy radiated per crossing, r_e is the classical particle radius, m is the particle rest mass, γ is the relativistic factor (proportional to the beam energy), N_1 and N_2 are the number of particles in beam 1 and beam 2 (proportional to the beam currents), and L_0 is the luminosity, as defined in Eq. 1.4. The dimensionless form factor $g(r)$ which results from the integration over space time is given by [16]:

$$g(r) = \frac{64\sqrt{\pi}r}{3\sqrt{3r^4 - 10r^2 + 3}} \arctan\left(\frac{\sqrt{3r^4 - 10r^2 + 3}}{3r^2 + 8r + 3}\right) \tag{2.4}$$

and depends on the beam aspect ratio $r = \frac{\sigma_y}{\sigma_x}$. For flat beams (in virtually any electron-positron collider), $r \ll 1$ and to a good approximation, $g(r) \approx 11.4r = 11.4\frac{\sigma_y}{\sigma_x}$. Substituting into Equation 2.2, σ_y cancels and the equation for total beamstrahlung power becomes:

$$W_1 = 11.4 r_e^3 mc^2 \gamma^2 \frac{f N_1 {N_2}^2}{4\pi\sigma_x^2\sigma_z} \tag{2.5}$$

which depends only on the beam energy, currents, σ_x, and σ_z. It is important to note the cubic current dependence (for beams with equal currents). A calculation using the CESR-c 2007 values listed in Table 1.1 shows that the total beamstrahlung power available at CESR-c is about 10 mW. Since this is much less than the synchrotron backgrounds due to the beam being off-axis in the quads near the IP, the wider angular spread of the beamstrahlung must be used to suppress the backgrounds to a more reasonable level.

2.3.2 Large Angle Power and Spectral Angular Distribution

2.3.2.1 Short Magnet Approximation

The radiation emitted must be treated using the short magnet approximation rather than the searchlight approximation used for normal synchrotron radiation because the observation angle θ, which is about 10 mrad in our experiment, is chosen to be much larger than the angle of the deflection in the beam-beam interaction, α, which is about 0.5 mrad. The situation is illustrated in Figure 2.1[17].

Hence large angle beamstrahlung can be considered a form of short magnet radiation, with interesting and useful properties first derived by Coisson [15]. The possibility of using SM radiation for beam-beam collision monitoring was suggested in [16]. This is the regime of interest for the purpose of this thesis.

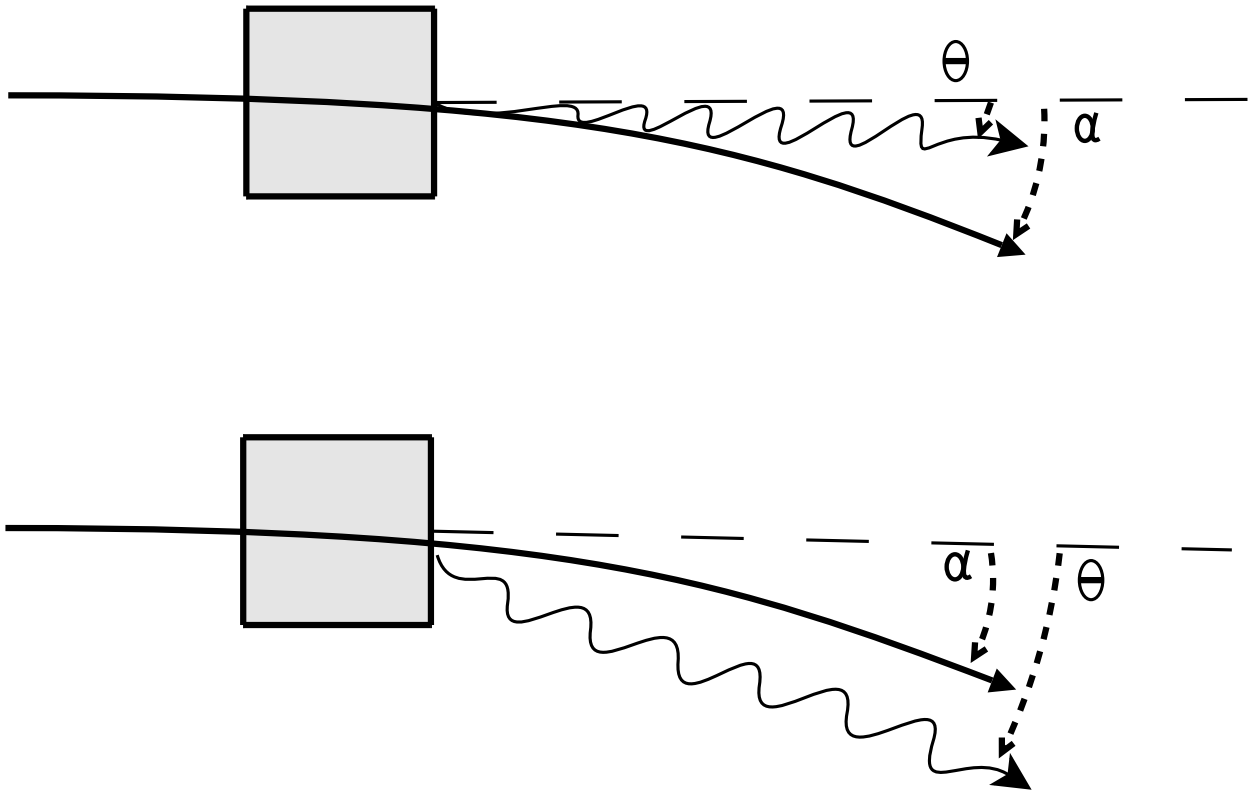

Figure 2.1: Top diagram shows the situation in which the searchlight approximation holds - the observation angle θ is less than the bending angle α. Bottom diagram illustrates the short magnet approximation case with the observation angle greater than the bending angle.

2.3.2.2 Short Magnet Spectral Angular Distribution

The spectral angular distribution of energy radiated by a particle in a single crossing of a short magnet is [16]:

$$\frac{d^2U}{d\Omega d\omega} = \frac{r_e\gamma^2 f_i(\phi,\theta)}{\pi c m c^2}\left|\tilde{F}\left(\frac{\omega(1+\gamma^2\theta^2)}{2c\gamma^2}\right)\right|^2 \tag{2.6}$$

with the differential solid angle $d\Omega = \sin\theta d\phi d\theta \approx \theta d\phi d\theta$, and angular frequency of the radiation ω. $\tilde{F}$ is the Fourier transform of the deflecting force $\mathbf{F}$ felt by the particles in the beam.

The short magnet approximation applied to the case of a beam-beam collision with two flat Gaussian beams, using the Fourier transform of the deflecting force yields two different angular distribution functions $f_i(\phi,\theta)$. The first one is f_σ for the polarization component with electric fields parallel or antiparallel to the deflecting force and the second is f_π for the polarization component perpendicular to the deflecting force. They are[16]:

$$f_\sigma(\phi,\theta) = \frac{(1-\gamma^2\theta^2\cos(2\phi))^2}{(1+\gamma^2\theta^2)^4} \tag{2.7}$$

$$f_\pi(\phi,\theta) = \frac{(\gamma^2\theta^2\sin(2\phi))^2}{(1+\gamma^2\theta^2)^4} \tag{2.8}$$

The beam-beam force is:

$$\mathbf{F}(x,y,z) = (\hat{F}_x(x,y), \hat{F}_y(x,y))\exp(-\frac{z^2}{2\sigma_z^2}) \tag{2.9}$$

Substituting the Fourier transform of the beam-beam force into Equation 2.6 and taking the case of observation angle $\theta \gg \frac{1}{\gamma}$ yields the average radiated power distribution by angle and frequency for each polarization component[16] (note factor of 2 correction [18]):

$$\frac{d^2P_x}{d\Omega d\omega} = \frac{3\sigma_z W_1}{2\pi\sqrt{\pi}c}\frac{g_x\cos^2(2\phi)+g_y\sin^2(2\phi)}{g(r)\gamma^4\theta^4}\exp\left(-\frac{\sigma_z^2\theta^4\omega^2}{16c^2}\right) \tag{2.10}$$

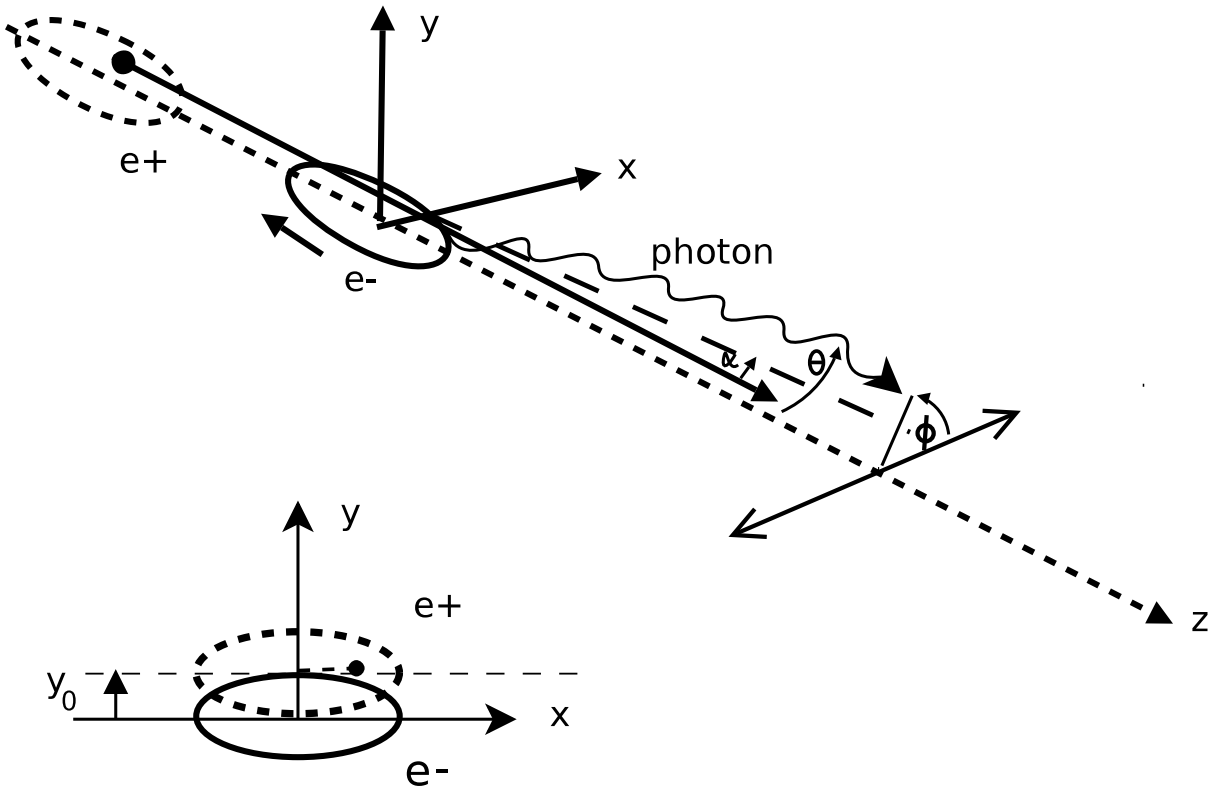

Figure 2.2: The geometry of large angle beamstrahlung given beams having a vertical separation y_0. α is the deflection angle, θ and ϕ are the components of the observation angle.

$$\frac{d^2P_y}{d\Omega d\omega} = \frac{3\sigma_z W_1}{2\pi\sqrt{\pi}c}\frac{g_y\cos^2(2\phi) + g_x\sin^2(2\phi)}{g(r)\gamma^4\theta^4}\exp\left(-\frac{\sigma_z^2\theta^4\omega^2}{16c^2}\right) \tag{2.11}$$

where P_x and P_y are the the x and y polarization components of the average radiated power for a single beam crossing, ϕ and θ are the solid angle components, and W_1 is given by Equation 2.5.

The functions g_x and g_y, which satisfy the equation $g_r = g_x + g_y$ when the beams overlap completely, are the form factor components due to horizontal and vertical deflection for flat Gausssian beams with a non-zero vertical separation y_0, and assuming that $y_0 \ll \sigma_x$ [16]:

$$g_x = \frac{8\pi r}{3\sqrt{3}}(\frac{1}{2} - R_x r) \tag{2.12}$$

$$g_y = \frac{8\pi r}{3\sqrt{3}}(\frac{1}{2}S(v) - R_y r) \tag{2.13}$$

with the functions defined as follows [16]:

$$R_x = \frac{2\sqrt{3}}{\pi}(exp(-v^2/2) + \sqrt{\pi/2}v \ \ \mathrm{erf}(v/\sqrt{2})) \tag{2.14}$$

$$R_y = \frac{2\sqrt{3}}{\pi}(exp(-v^2/2) + \sqrt{2\pi}v \ \ \mathrm{erf}(v/\sqrt{2})) \tag{2.15}$$

$$S(v) = \frac{3}{\sqrt{\pi}}\int_{-\infty}^{+\infty} exp(-(u-v)^2)\mathrm{erf}^2(u)du \tag{2.16}$$

All of these are functions of the normalized separation $v = y_0/\sqrt{2\sigma_y}$. S(v) ranges from a minimum $S(0) = 1$ to a limiting value of 3 for v large.

The large angle beamstrahlung power emitted by the beam-beam collision may be calculated by integrating Equation 2.10 and Equation 2.11 over the solid angle Ω and the spectrum $\Delta\omega$ of interest. The signal tables in Chapter 5 were calculated by numerical integration of Eqs. 2.10 and 2.11 over the angular acceptance and the frequency range of the detector, with a normalized separation $v = 0$ using a look-up table of quantum efficiency values provided by Hamamatsu and one of S(v) values calculated numerically for a 0-10σ_y range of v values. Because the quantum efficiency for the PMTs as given by Hamamatsu is a function of wavelength, Eqs. 2.10 and 2.11 require the differential replacement

$$d\omega = \frac{2\pi c}{\lambda^2}d\lambda$$

to convolute the power spectrum with the PMT quantum efficiency curves.

When observed at a fixed angle θ, the emitted radiation has a Gaussian spectrum with

rms angular frequency ω_{rms} and rms wavelength λ_{rms} given by [16]:

$$\omega_{rms} = \frac{2\sqrt{2}c}{\sigma_z \theta^2}, \qquad \lambda_{rms} = \frac{\pi \sigma_z \theta^2}{\sqrt{2}} \tag{2.17}$$

2.4 Large Angle Beamstrahlung Key Characteristics

2.4.1 Summary Listing

The following characteristics of large angle beamstrahlung are noteworthy:

1. The radiated power is a minimum for perfectly aligned beams.

2. The radiated power has a $1/\gamma^2$ dependence.

3. The radiation becomes strongly linearly polarized as the vertical separation increases and the bending force becomes primarily vertical. This polarization has an eight-fold pattern around the azimuth, as shown in Figure 2.4.1. The opposite polarization pattern will result from a strong horizontal separation.

4. The radiated power has a clear dependence on both σ_z and σ_x.

5. The spectrum observed at a fixed angle depends only on σ_z.

6. The radiated power has a cubic dependence on the currents.

2.4.2 Characteristics in Detail

The first characteristic, perfect alignment yields minimum beamstrahlung, could be used to check and maintain alignment of the beams, thus achieving consistently less wasted luminosity and avoiding beam loss. The position of minimum beamstrahlung power is the position of best alignment. This is also true for other types of misalignments, including horizontal, asymmetric beam cross-sections and one beam rotated with respect to the other.

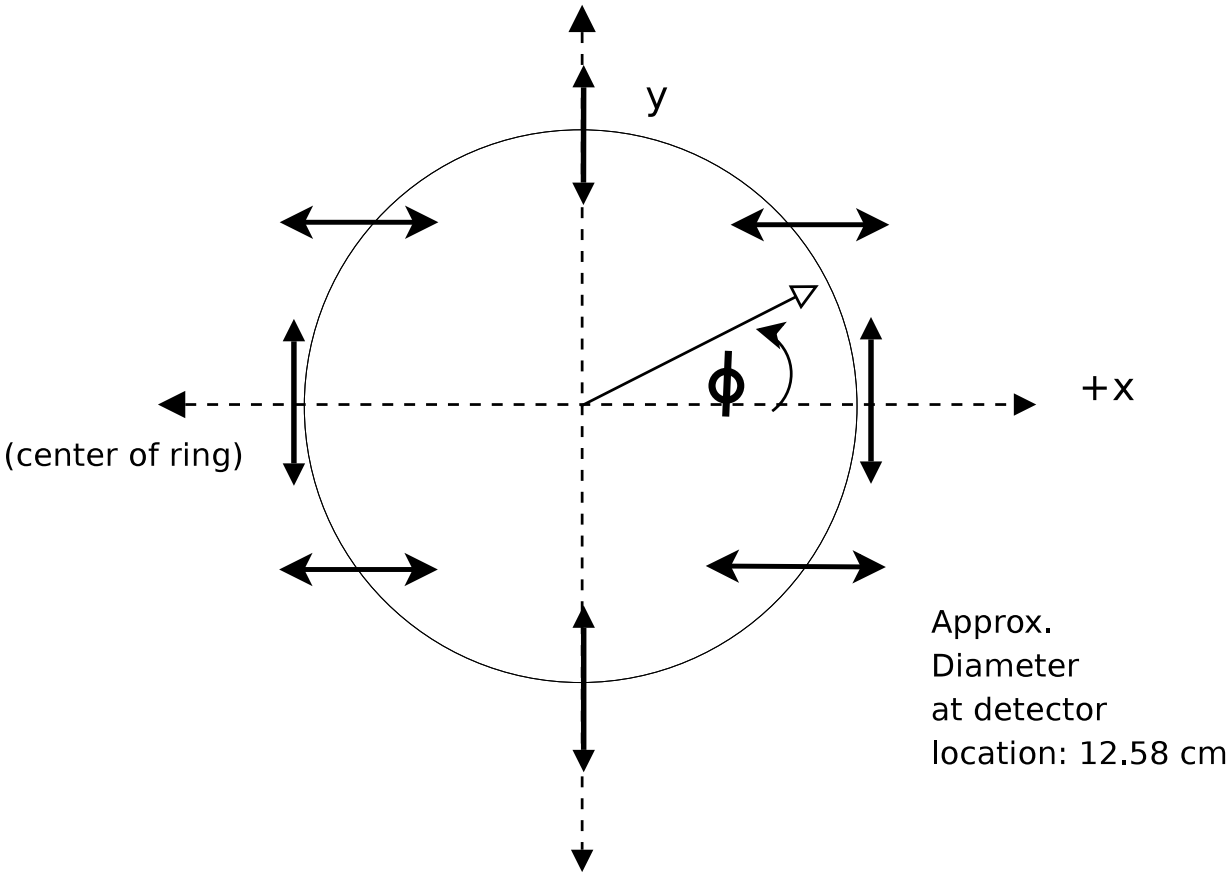

Figure 2.3: Cross-section of the CESR beampipe at detector window location, 5.92 m from the IP, illustrating the polarization of beamstrahlung due to vertical bending varying with location in azimuth - an 8-fold polarization pattern.

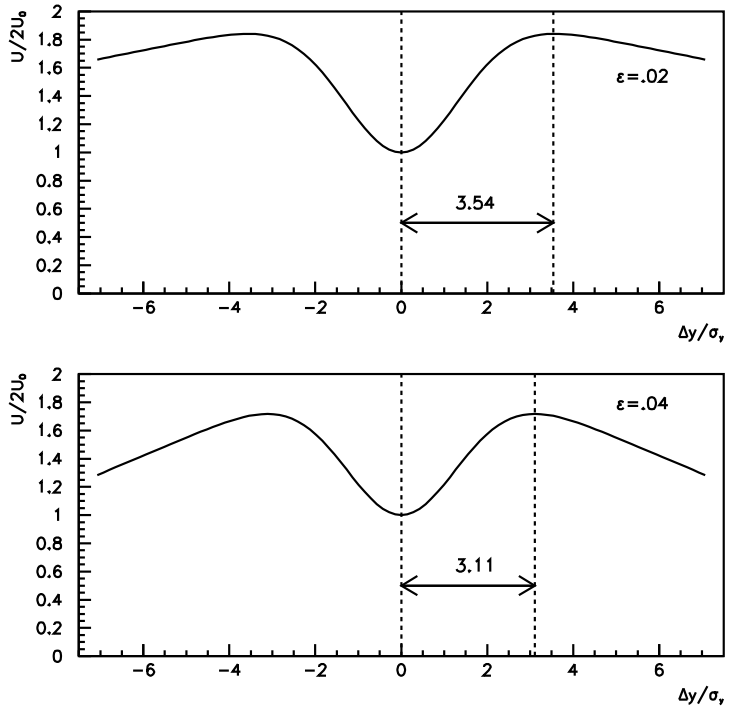

Figure 2.4: Plots of normalized beamstrahlung power vs. normalized vertical separation for two different aspect ratios ($\epsilon = \frac{\sigma_y}{\sigma_x} = 0.02$ and 0.04). Note the characteristic "camelback" shape, with minimum beamstrahlung power at the point corresponding to zero separation.

For the case of vertical misalignment, this is illustrated by a "Camelback" diagram of total power U vs. v, the beam-beam offset, produced by a scan of one beam along the vertical axis as shown in Figure 2.4.2[17]. Such a scan could also be used to measure the beam height σ_y. A similar technique could be used to measure σ_x [2].

The second characteristic, the $\frac{1}{\gamma^2}$ dependence, indicates that the large angle beamstrahlung signal becomes stronger at lower energies, which means that conditions for beamstrahlung detection are still favorable at CESR-c despite the fact that typical energies are no more than forty percent of what they were under CESR Phase III conditions in the 1990s.

The third characteristic, polarization, provides much more information about the beam-beam collision than total beamstrahlung energy alone. It has been suggested that the polarization information in the form of two normalized vectors $\mathbf{U_1}$ and $\mathbf{U_2}$, proportional to the form factors g_x and g_y, could be plotted together to form a beamstrahlung diagram [2]. In

such a diagram, a perfect collision is indicated by the two vectors equal in length and overlapping perfectly. Any discrepancy from this would indicate that alignment problems exist, causing wasted luminosity. In principle, a beamstrahlung detector could produce the beamstrahlung diagram on a monitor in the control room and and then as alignment problems are perceived, adjustments could be made until the diagram indicates good alignment.

The fourth characteristic, σ_z and σ_x dependence of the total power, provides two other important quantities which could be monitored by means of a beamstrahlung detector, providing additional information about the beam-beam collision and therefore the optimization of luminosity.

The fifth characteristic, the spectral dependence on σ_z, could possibly be exploited to monitor this important quantitity, which in turn would aid in monitoring σ_x, since the total power depends on both.

The sixth characteristic, the cubic current dependence, is actually $I_1 I_2^2$ where I_1 is the current of the radiating beam and I_2 is the current of the deflecting beam. This is important for background discrimination in general, and in particular, for the type of preliminary signal search that is the focus of this thesis. The backgrounds are primarily synchrotron radiation from the beams being off-axis in the focusing superconducting quadrupole magnets near the IP. Such radiation has a linear dependence on the current, so as the currents naturally decrease over the course of a run, it should be possible to discriminate the relatively small beamstrahlung signal from the larger synchrotron backgrounds by means of their different dependence on the currents: cubic vs. linear.

Chapter 3

The Detector

3.1 Overview

This chapter gives details of the design, construction, and operation of the unique prototype large angle beamstrahlung detector installed and operating at CESR by Mikhail Dubrovin, a post-doc working under the direction of Giovanni Bonvicini of Wayne State University. As discussed in Chapter 2, beamstrahlung radiation is produced at CESR via the beam-beam interaction at the IP. Under current High Energy Physics (HEP) operating conditions at CESR with energy of about 2 GeV per beam (details in Chapter 1), and observed at large angles ($\theta \gg \frac{1}{\gamma}$), the large angle beamstrahlung signal is predominantly at wavelengths$\lambda \geq 800$ nm. The detector comprises an optical path for large-angle (≈ 10 mrad) beamstrahlung radiation in the visible to near-infrared (NIR) range, optical components for extraction of polarization information, two band wavelength discrimination (visible and near-infrared), and photon counting. The detector collects light at two locations, one on the East side of the interaction point (IP) (looking at the beamstrahlung radiation from the incoming electron beam) and one on the West side of the IP (looking at the beamstrahlung radiation from the incoming positron beam). Data taking is integrated into the CESR control system, enabling beamstrahlung photon counting concurrent with the recording of CESR parameters

such as luminosity and beam currents.

3.2 The Optical Path

The following description applies to installations on both the East and West side of the IP. Beamstrahlung radiation produced at the IP travels a distance of approximately 5.92 m down the beam pipe where a small fraction is reflected by twin 45° copper mirrors (CM) mounted on the inside of the beam-pipe, separated by a gap of 1.53 cm, and having an effective total cross-sectional area of about 1.28 cm^2. The mirrors are arranged so that the center of the two mirrors are separated by 22.5 degrees in azimuth. The 8-fold azimuthal pattern described in Chapter 2 is sampled with half-periodic azimuthal distance between the two mirrors.

The CMs are located at a point where the beam-pipe is round and has an inside radius ≈ 6.3 cm. With respect to the IP, their inner edge is located about 9.2 mrad from the beam pipe axis, and the outer edge at approximately 10.4 mrad. However, the beams enter the IP region at a non-zero crossing angle, pointing inward with respect to CESR. The mirrors are on the outward side of the beam pipe with respect to CESR. The beamstrahlung observation angle (with respect to the radiating beam) is roughly 10.4 to 10.6 mrad at the inner edge of the mirrors, depending on the exact observation angle, and at the outer edge it is 1.1 to 1.2 mrad greater.

The CMs are positioned on the inner surface of the beam pipe at an azimuthal angle of $-72.5°$ and $-50°$ as measured azimuthally from the outer point on the beam pipe (they are on the lower, outer part of the beam pipe).

These locations were chosen primarily on the basis of a study of the synchrotron radiation backgrounds[2], which had been performed for 5 GeV beams at CESR. The backgrounds at 2 GeV, however, are much stronger at the $-50°$ location, than previous simulations indicated. Given the large dynamic range of the beamstrahlung rates, it was found convenient to use the

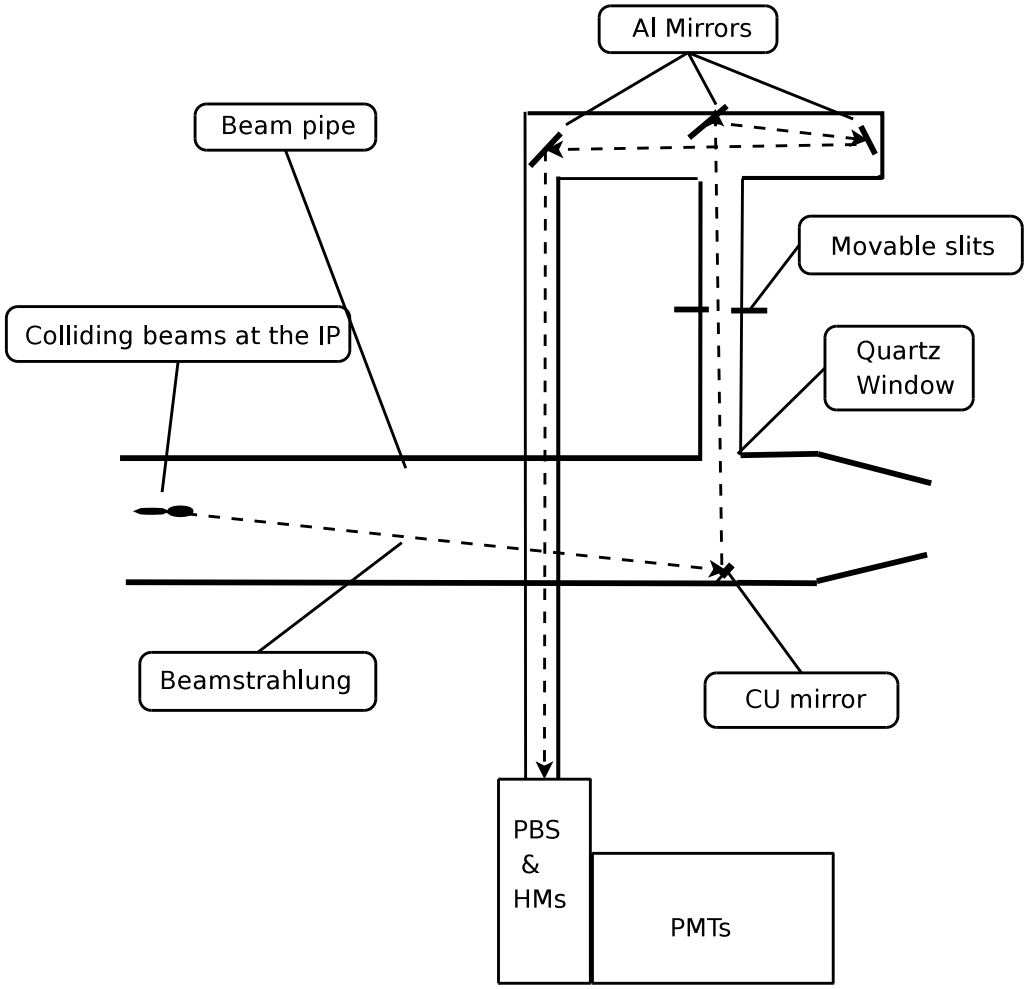

Figure 3.1: The optical path of the beamstrahlung detctor, South view.

electronic channels observing the -50° location to measure the 0.1 Hz rates at the -72.5° location. Therefore, the current data stream has both 1 Hz and 0.1 Hz rates at -72.5°, but no -50° data.

The reflected light exits the beam-pipe through twin 0.276 in square quartz windows, entering the light-tight optical path. Next the light is collimated by means of a pair of movable slits. As the light beam propagates the ≈ 6 m length of the path extension volume as shown in Fig. 3.1, it is reflected three more times, restoring the original polarization. Polarization information is extracted using a polarizing beam splitter (PBS). The two polarization components each encounter a hot mirror (HM), before entering the appropriate

photomultiplier tube (PMT). Thus the initial beamstrahlung signal is divided into 4 parts, first by polarization and then by color (Figures 3.2 and 3.3).

3.3 Collimation via Movable Slits

Two movable slits 5 mm wide, one horizontal, one vertical, whose intersection compose a positionable square aperture, allow the operator to select the observation angle. It is also possible to position the slits so that there is no collimation (open), or no aperture (closed). A stepper motor moves a slit by means of a $\frac{1}{4}$ in threaded shaft with 28 threads per inch, 400 steps per revolution. The motors use CESR style controllers. Each slit is constrained to slide in a channel within the optical volume. Slit position is controlled remotely during CESR operations through the CESR control computer system.

3.4 Optical Elements

The optical path extension volume is constructed of 4 in o.d. and 1 in o.d. aluminum alloy optical tubing, threaded fittings, and end caps. An elliptical mirror located above the movable slits reflects the light to a circular mirror, which reflects the light to another elliptical mirror, extending the path from IP to the PMTs to a total length of $\approx$ 12 m. These mirrors are $\frac{1}{8}\lambda$ Enhanced Aluminum (Edmund Optics). The final path segment is constructed out of 1 inch o.d. aluminum optical tubing. The light then enters a Glan-Taylor calcite polarizing beam splitter (PBS), which has a square cross-sectional area of 1 cm^2. The PBS is oriented so that the horizontal (x) and vertical (y) polarization components are extracted. Two 1 cm^2 Borosilicate Hot Mirrors (HM) (Edmund Optics, R43-955) are positioned to divide the x and y polarization components by color. With a 45° angle of incidence, the ranges are: transmission 300–650 nm (nominally VIS) and reflection: 650–1100 nm (nominally NIR). This provides 4 channels on each side of the IP: 4 West and 4 East for a total of 8 channels. The light entering the R2228 PMTs is filtered with a X-Nite780 Infrared Pass filter, which

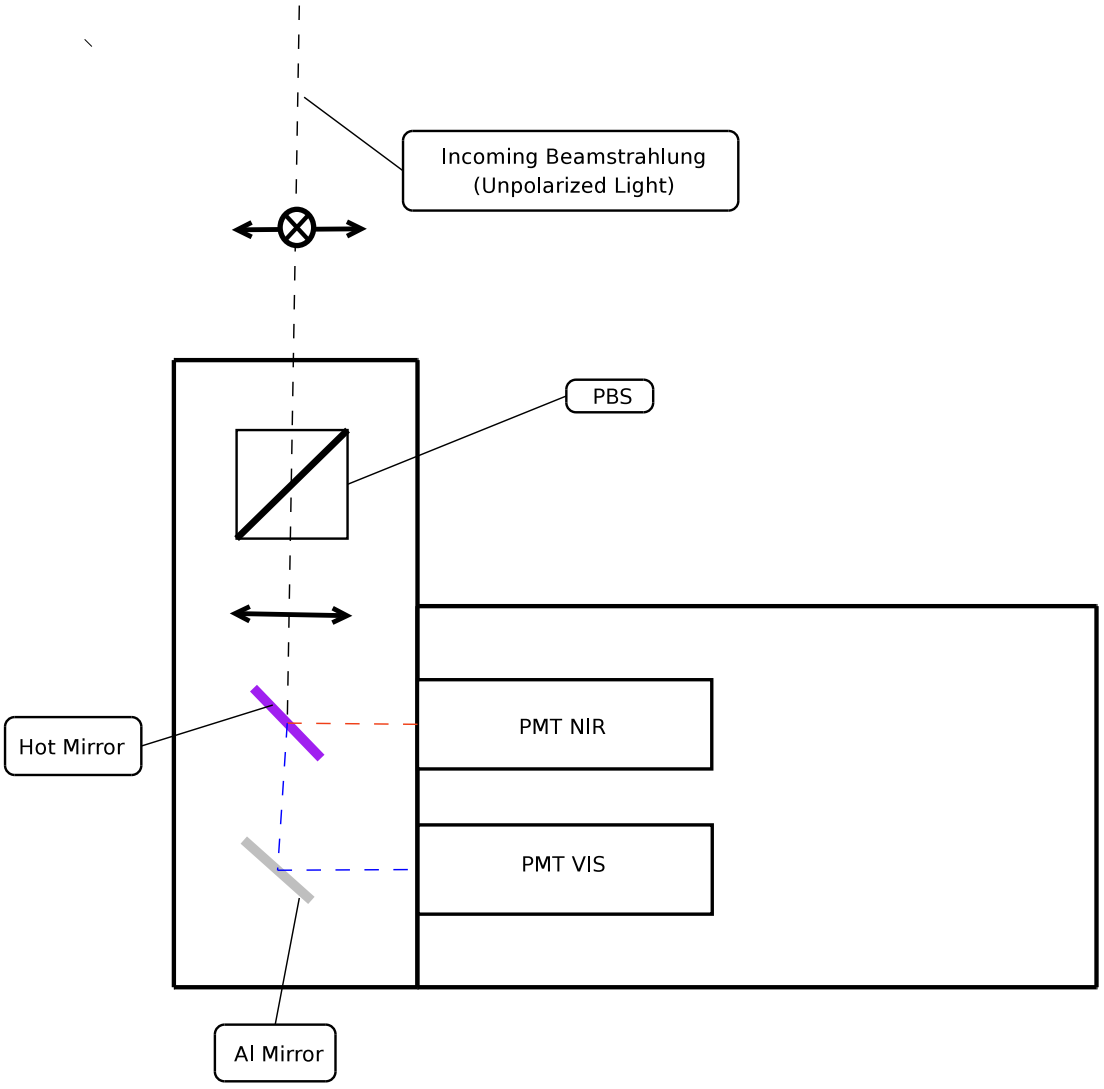

Figure 3.2: Detail of beamstrahlung detector, South view: components include polarizing beam splitter (PBS), hot mirrors (HM), and photomultiplier tubes (PMT)

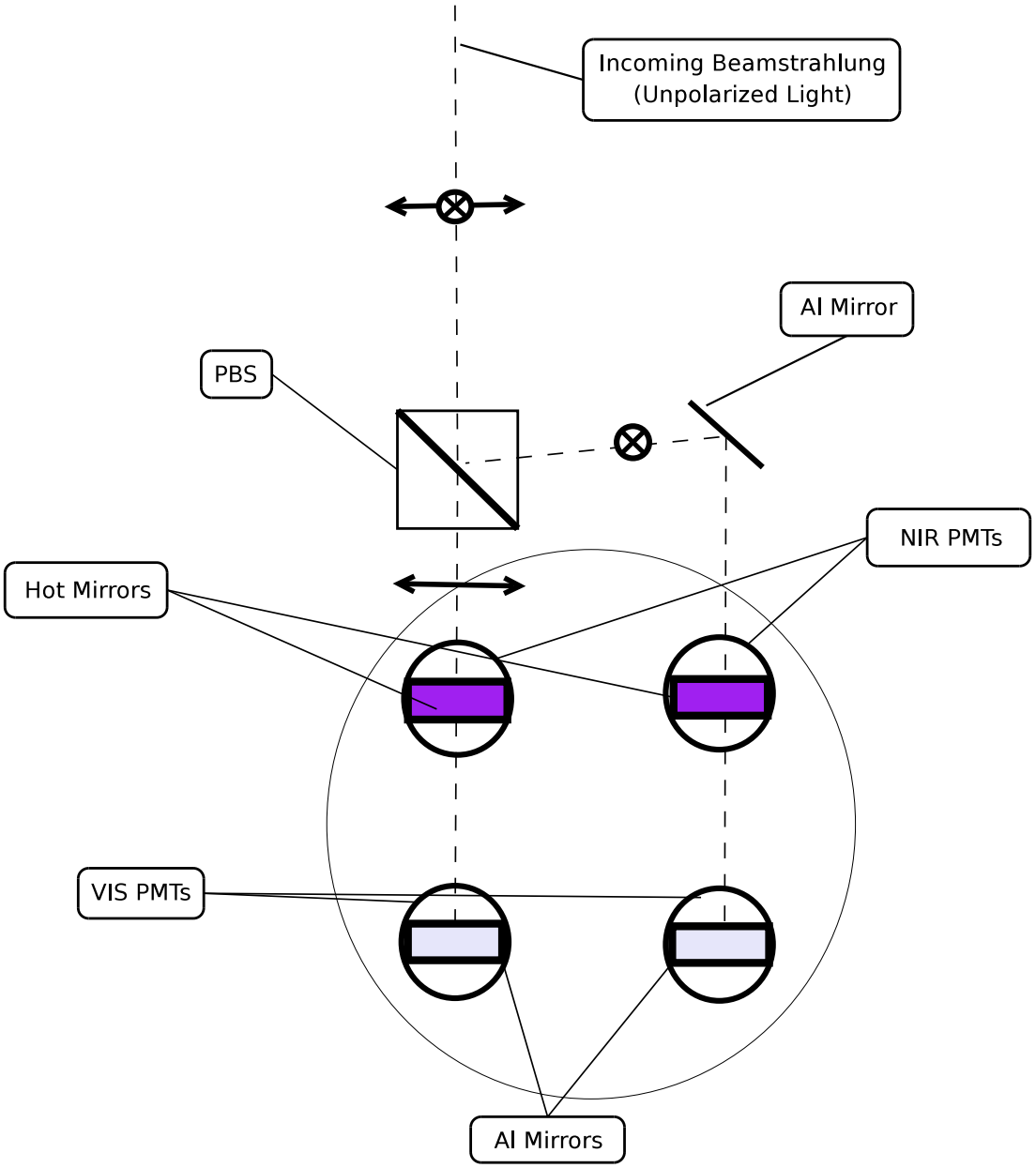

Figure 3.3: Detail of beamstrahlung detector, East view: components include polarizing beam splitter (PBS), hot mirrors (HM), and photomultiplier tubes (PMT)

passes wavelengths in the range 780–1000 nm.

3.5 Photomultipliers (PMTs)

All PMTs are from Hamamatsu. We have employed three different models. The R6095 bialkali for detection in the VIS range, the R316-02 bialkali for detection in the NIR range, and the R2228 extended red multialkali, also in the NIR range. All tubes have a diameter of 28 mm with a photo cathode diameter of 25mm. The R6095 is sensitive in the range 300-650 nm with maximum response at 420 nm. The R6095 monitors the synchrotron radiation backgrounds only, with very little if any signal occurring in this range. The R2228 is sensitive in the range 300-900 nm with maximum response at 600 nm. The R2228 combined with the X-Nite780 filter is sensitive to the range 780-900 nm. This combination provides a primary source of background rejection. The R2228s were chosen and installed to replace the R316-02 PMTs, also from Hamamatsu, which have a similar range of detection, but require cooling and have a lower quantum efficiency.

The (currently decommissioned) R316-02 (NIR) is sensitive in the range 400-1200 nm with maximum response at 800 nm. R316-02 combined with the red dichroic filter receives the NIR range from 700-1100 nm. R316-02 has a high dark current (2000-5000 nA at 25 ° C compared to 2-10 nA for the R6095 and 8-30 nA for the R2228) and therefore requires cooling to $\leq -50\,^{\circ}\mathrm{C}$. The cooling system uses LN2 circulated through aluminum tubing in contact with aluminum heat sinks in the space near the R316-02, and the remaining space filled with polyurethane foam thermal insulation. The LN2 flow from a 30 L Dewar is monitored with a rotameter and pressure is passively provided by means of the thermal gradient. Thermal sensors monitor the temperature at two locations, which is included in the data record. The gaseous nitrogen with its thermal load is exhausted into the surroundings. With a full Dewar (23 kg LN2), the device can run for about 20 hours at $\leq -50\,^{\circ}\mathrm{C}$.

The PMTs are located in a low magnetic field region, and each PMT is individually

shielded from magnetic fields by a housing of soft iron. PMT electronics include high voltage power supply (ORTEC Model 556), constant fraction discriminator (ORTEC CF8000), and CESR online control electronics.

3.6 Computer Control and Data Taking

The detector is hardwired into the CESR control system, in accordance with lab policy. The general procedure for data taking is to check the status of the beam to ensure favorable conditions exist, log onto the CESR control system and run a program to position the movable slits, then run another program for online data taking, which writes records up to once every 2 seconds, for a period of time specified by the user. The records include the slit positions, photon counts recorded in the interval, temperature, CESR currents, luminosity data, and other data gathered via the CESR online information sources. Currently the setup includes 2 channels for each PMT, taking data at a nominal 1 Hz rate and 0.1 Hz rate simultaneously. This provides a backup in case any of our counters is overwhelmed to the maximum.

Chapter 4

Beam Dimensions and Observation Angle Calculations using CLEO Timelines Data

4.1 About CLEO Timelines

The CLEO detector is a sophisticated multifaceted HEP detector, an integral part of the particle physics program at Cornell University's LEPP. The CLEO Timelines data base is a repository of a vast array of measurements made by the detector, including some which are relevant to our studies: rms beam sizes and the beam crossing angle[19]. In this chapter is presented the rationale for and derivation of methods we used for the analysis of CLEO Timelines data in order to obtain some of the important quantities required for use in the characterization and computation of expected beamstrahlung signal rates.

4.2 Notation and Overview of the Calculation

We calculated the rms beam dimensions at the IP σ_x^2 and σ_z^2 using CLEO Caliper Beamspot width (CB width) data made available through CLEO Timelines. These CB

widths are the convolution of the physical size of the beamspot with the detector resolution [19]. To distinguish CB widths from the beam sigmas, I will use the notation, σ_{xCB}, for example. The detector measures the size of the luminous region in three dimensions and from this measurement we can calculate the transverse and longitudinal beam dimensions. The detector resolution is determined from the measurement of the σ_{yCB}, which is then used in calculating the beam dimensions, σ_z and σ_x.

Recall that at CESR (as well as in every other e^+e^- machine) beam sizes at the IP are such that $\sigma_z >> \sigma_x >> \sigma_y$. Further, $\sigma_y << \sigma_{yCB}$, and, due to the cylindrical symmetry of the CLEO detector, one may safely assume that $\sigma_{xCB} = \sigma_{yCB}$. Thus, the σ_{yCB} measurement is taken as a measurement of the CLEO resolution. σ_y is then measured using the method discussed in Chapter 3.

4.3 Derivation of Beam Dimensions from Caliper Beamspot via Luminosity

The relation between the "true" rms beam size and the measured CB width of the luminous region may be found by examining the expression for the luminosity. Recalling Equation 1.2 from Chapter 1, the luminosity L_{sc} for a single beam crossing is:

$$L_{sc} = 2c \int dV d\tau \rho_1(\mathbf{r}, \tau)\rho_2(\mathbf{r}, \tau), \tag{4.1}$$

where the volume element $dV = dxdydz$ and τ is a time variable of order of the beam-crossing duration. Assuming perfect overlap of two Gaussian beams, then for a single beam crossing:

$$L_0(\tau) = \frac{2N_1(\tau)N_2(\tau)c}{(2\pi)^3\sigma_x^2(\tau)\sigma_y^2(\tau)\sigma_z^2(\tau)} \int dV d\tau e^{-(x^2/\sigma_x^2(\tau)+y^2/\sigma_y^2(\tau)+(z^2+(c\tau)^2)/\sigma_z^2(\tau))} \tag{4.2}$$

where the $N_{1,2}$ and $\sigma_{x,y,z}$ are the beam populations and spatial dimensions at any given time τ. In principle, the Caliper Beamspot algorithm measures $\frac{\partial L}{\partial x}$, $\frac{\partial L}{\partial y}$ and $\frac{\partial L}{\partial z}$. The expression for the latter is:

$$\frac{\partial L}{\partial z} = Ke^{-(z^2)/\sigma_z^2(t)} \int dxdyd\tau e^{-(x^2/\sigma_x^2(t)+y^2/\sigma_y^2(t)} \tag{4.3}$$

the remaining integral results in a constant so essentially

$$\frac{\partial L}{\partial z} = Ae^{-(z^2)/\sigma_z^2(t)} \tag{4.4}$$

Rewriting the exponent:

$$\frac{\partial L}{\partial z} = Ae^{-z^2/2(\frac{\sigma_z^2}{2})} \tag{4.5}$$

It is obvious that $\frac{\partial L}{\partial z}$ is a Gaussian with $\sigma^2 = \sigma_z^2/2$. Thus the true beam length is related to the Caliper Beamspot width by $\sigma_z = \sqrt{2}\sigma_{zCB}$. The analysis for x and y is similar, yielding $\sigma_x = \sqrt{2}\sigma_{xCB}$. Detector effects are discussed in the next Section.

4.4 Drift Chamber Detector Resolution

The Caliper package measures the 3-dimensional location of the fitted interaction point in hadronic events in the CLEO detector, by propagating each track reconstructed in the CLEO Drift Chamber back to the IP. A fitting routine finds the point in space which has a minimum overall distance from the tracks, and this point is designated to be the interaction point for this event. The 3-D map of the interaction points is then used to extract the lateral and longitudinal spreads of the luminous region[19].

The drift chamber is composed of thousands of wires and the resolution is a function of the wire spacing. These wires are mostly axial, and they measure best the x and y (transverse) coordinates of the charged tracks. The longitudinal coordinate z is measured by stereo wires at a shallow angle. This results in a factor of 4 worse longitudinal resolution with respect to the transverse resolution, but this results in a change of less than 1% of σ_z,

due to the difference in scale mentioned above. The detector resolution which we will call σ^2_{CLEO} is $\approx \sigma^2_{yCB}$. The full equations used to extract the measured beam parameters are:

$$\frac{\sigma_x^2}{2} = \sigma^2_{xCB} - \sigma^2_{CLEO} \tag{4.6}$$

$$\frac{\sigma_z^2}{2} = \sigma^2_{zCB} - 4\sigma^2_{CLEO} \tag{4.7}$$

The beam size calculations were done using the averages from plots made using CLEO timelines for the periods August 12-20, 2006 (Figures 4.1 and 4.2) and September 11-17, 2006 (Figures 4.3 and 4.4). The results are in Table 4.1. Using an accepted value of $\sigma_y \approx 7\mu$m (2006 HEP conditions), σ_{yCB} is approximately the detector resolution in y: $\sigma_{CLEO} \approx$ 0.22mm.

Period	σ_{xCB} (mm)	σ_{zCB} (mm)	σ_x (mm)	σ_z (mm)
Aug 14-20, 2006	0.341	7.60	0.367	10.7
Sep 11-17, 2006	0.361	7.75	0.403	10.9

Table 4.1: Beam Dimensions Calculated from CLEO Timelines Caliper Tracking Beamspot widths averages

The 2007 beam dimensions values used in the expected rates calculations in Chapter 5 were also obtained in this manner.

4.5 Detector Observation Angle Dependence on Beam Crossing Angle

As discussed previously, CESR beams collide with a small (on the order of a few milliradians) horizontal crossing angle. In order to calculate the observation angle θ_{obs} for normal HEP conditions with a non-zero crossing angle consider the following analysis. The solid angle subtended by our detector window is $d\Omega = \sin\theta d\theta d\phi \approx \theta d\theta d\phi$ (for $\theta \ll 1$). Using a

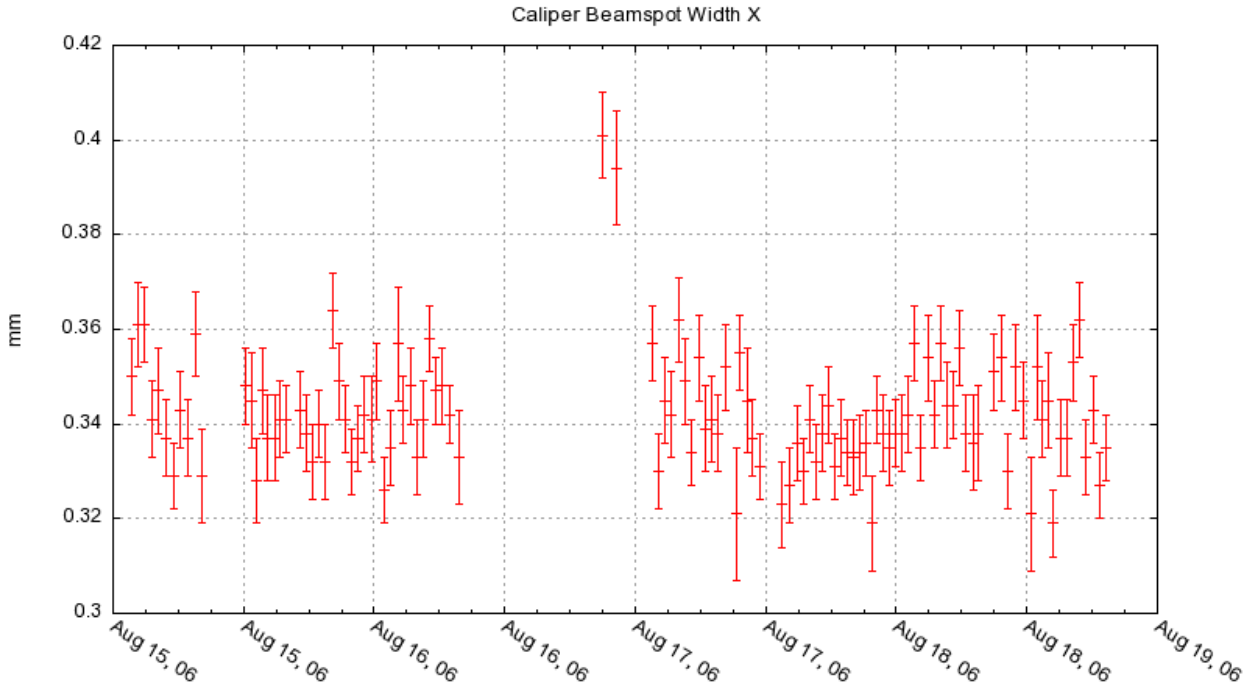

Figure 4.1: Beamspot width in x from Caliper Tracking in CLEO Timelines, 150 runs, August 15-19, 2006

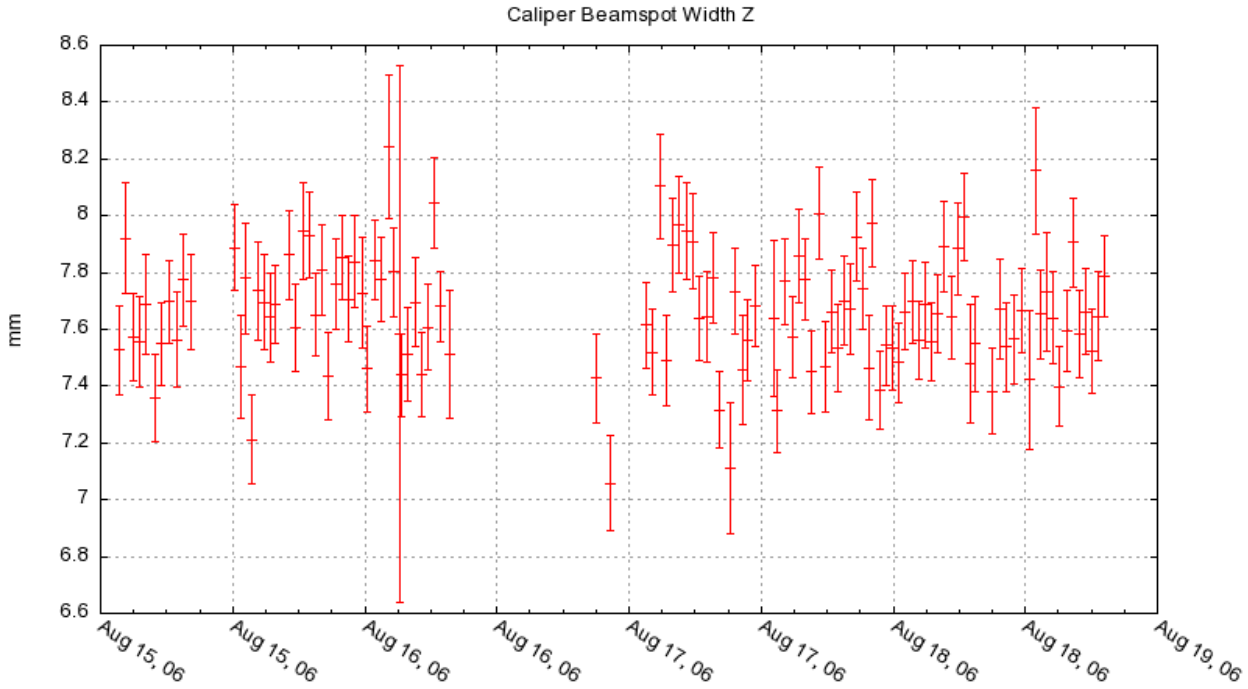

Figure 4.2: Beamspot width in z from Caliper Tracking in CLEO Timelines, 150 runs, August 15-19, 2006

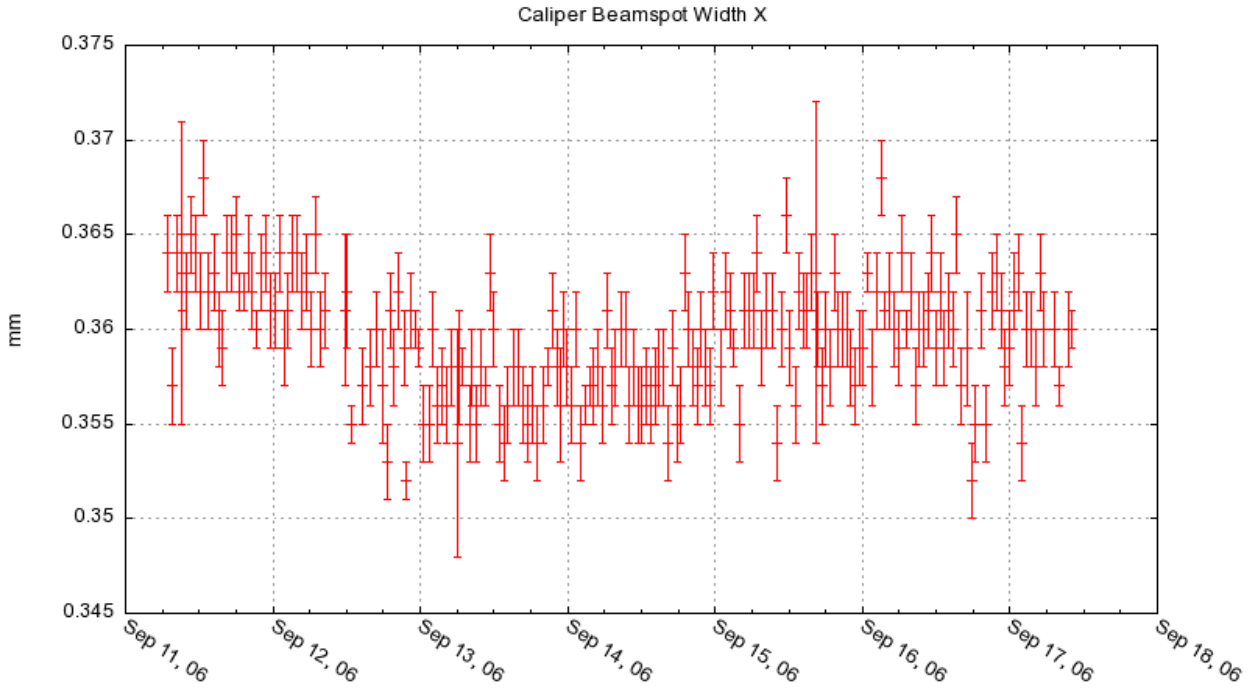

Figure 4.3: Beamspot width in x from Caliper Tracking in CLEO Timelines, 150 runs, September 11-18 2006

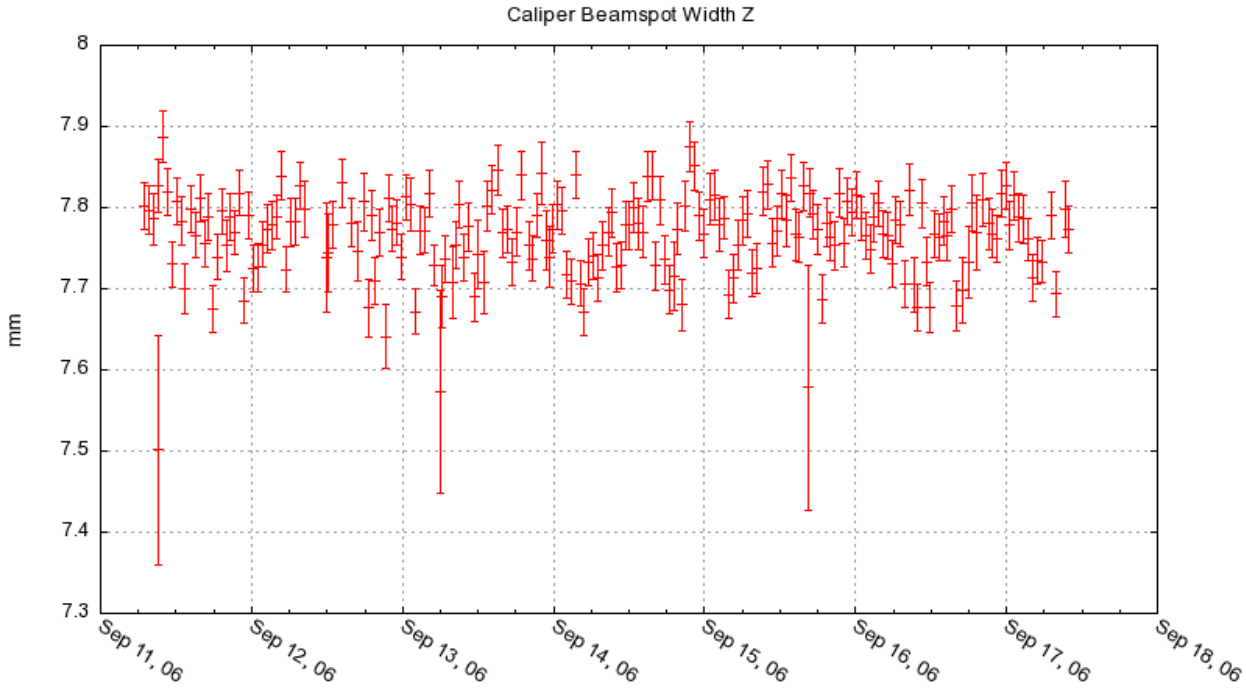

Figure 4.4: Beamspot width in z from Caliper Tracking inCLEO Timelines, 150 runs, September 11-18 2006

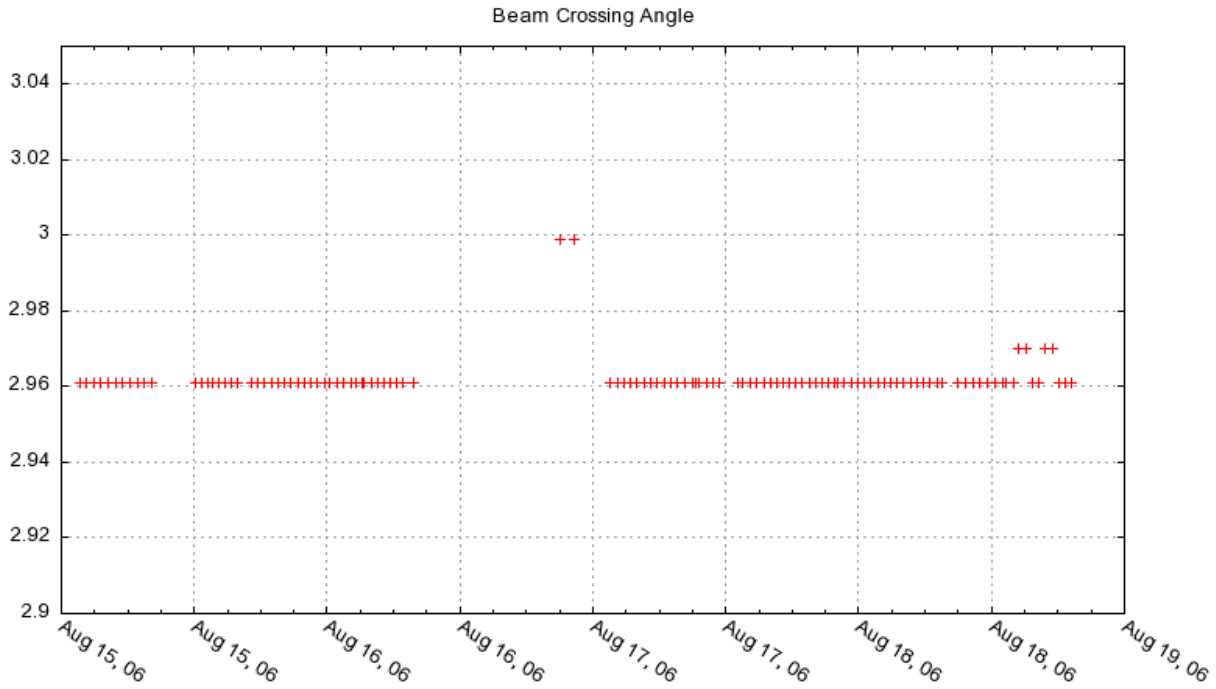

Figure 4.5: Plot of beam crossing angle from Caliper tracking, CLEO Timelines, 150 runs, August 15-19, 2006

two-dimensional approximation, we can think of θ as a vector with two components:

$$\theta_x = \theta \cos\phi \tag{4.8}$$

$$\theta_y = \theta \sin\phi \tag{4.9}$$

$$\theta = \sqrt{\theta_x^2 + \theta_y^2} \tag{4.10}$$

To account for the crossing angle which is in x only, we define $\theta'_x = \theta_x + \theta_{cross}$ and $\theta'_y = \theta_y$. Substituting these into Equation 4.10, we get, for the case of a beam with a crossing angle,

$$\theta_{obs} = \sqrt{(\theta \cos\phi + \theta_{cross})^2 + (\theta_y \sin\phi)^2} \tag{4.11}$$

As mentioned above, the crossing angle varies somewhat over time, though usually not much from one run to the next.

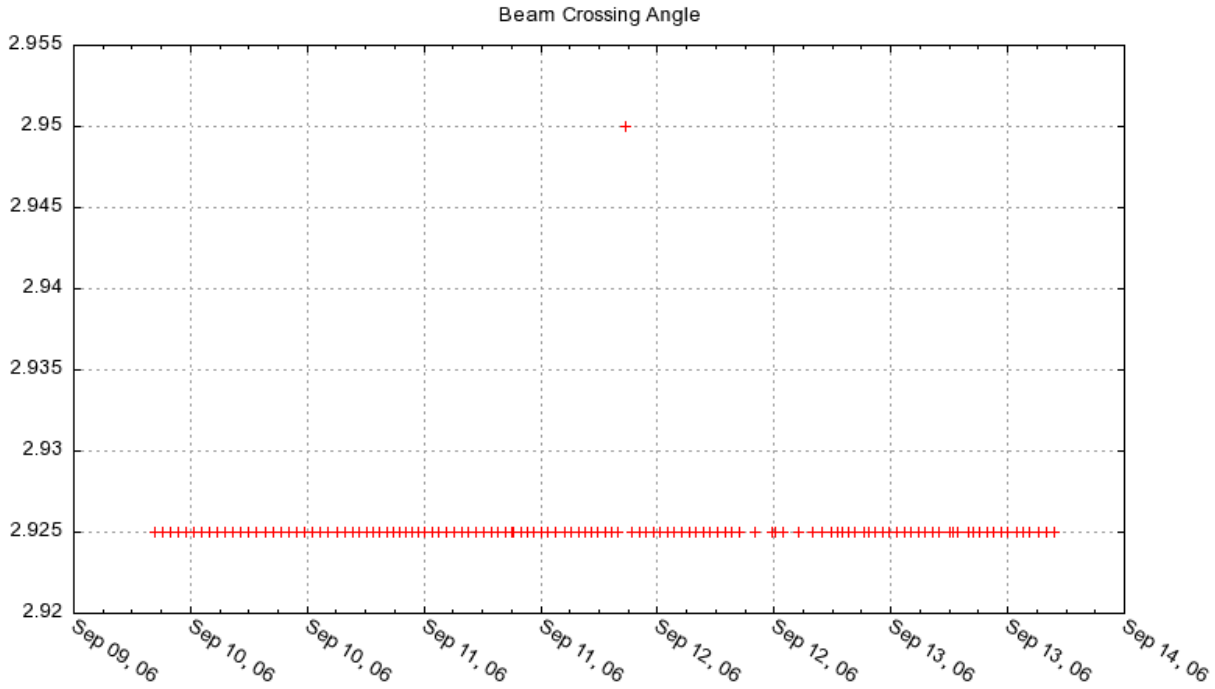

Figure 4.6: Plot of beam crossing angle from Caliper tracking, CLEO Timelines, 150 runs, September 9-14, 2006

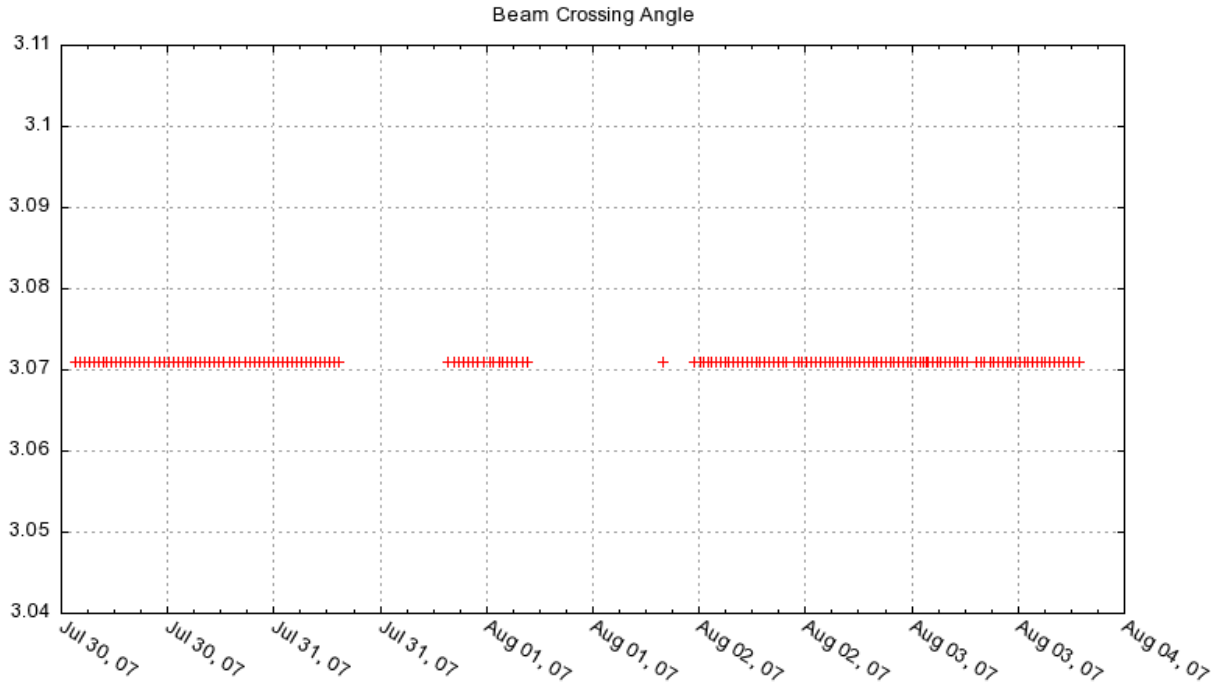

Figure 4.7: Plot of beam crossing angle from Caliper tracking, CLEO Timelines, 150 runs, July 30 - August 4, 2007

Figures 4.5, 4.6, 4.7 are plots which were produced using data from CLEO Timelines. The plots show that from run to run (each point represents one run), the crossing angle remains quite stable within these plots which include 150 runs each. Each plot encompasses a time period of several days and the duration of a run is roughly about 30 minutes. A comparison of the three plots for distinct periods of time during 2006-2007 shows that the average crossing angle can and does vary significantly, up to a level of about 5%.

Chapter 5

Expected Beamstrahlung Rates at CESR

5.1 About the Calculations

The tables herein summarize the calculated yields for beamstrahlung detection at CESR along with some important parameters used for those calculations. The expected rates were obtained via numerical integration of Equations 2.10 and 2.11 [16], with wavelength-dependent PMT quantum efficiencies applied by means of a look-up table using data provided by the manufacturer. As discussed in Chapter 3, the PMTs we have employed are Hamamatsu R6095 (nominally visible, with a range of sensitivity of $\lambda \approx 240 - 650$nm), Hamamatsu R316-02 and Hamamatsu R2228 (nominally near infrared, with a range of sensitivity of $\lambda \approx 650 - 1000$nm). Hammamatsu R316-02 (also nominally near-infrared with a similar window of detection to the R2228) is included for historical purposes, but has been decommissioned at the time of this writing. The rates are in units of the number of photons counted per second.

5.2 Rate Table Organization and CESR Parameters

Tables 5.3-5.18 summarize the results for various configurations of parameters representative of CESR-c HEP conditions for the time period September 2006 - August 2007, both without and with a convoluted angular divergence factor (indicated by "w/CAD"). The calculation is then repeated for a triangular acceptance. The parameters which are varied are the energy per beam and the beam dimensions in x and z (σ_x and σ_z). Parameters are varied one at a time, the first 8 tables are for the 2.1 GeV per beam energy (representative of HEP running during Fall 2006), the last 8 are with 1.89 GeV per beam energy (representative of HEP running during July-October 2007). The beam dimensions used are averages obtained from analysis done using the CLEO Timelines, details in Chapter 4.

5.3 Detector Parameters

The slit size is 5 mm^2. The slit is positioned with its "innermost" edge at the location corresponding to an angle of θ_{min} mrad and it extends from there to about $\theta_{min} + 0.85$ mrad, so there is a good bit of overlap within the tables. Rates are for an individual PMT, looking at only one polarization, with either the e^+ or the e^- as the radiating beam, at -72.5 degrees in ϕ. The window for detection of large angle beamstrahlung light at CESR with our current setup is roughly $650 < \lambda < 900$ nm, due in large part to the angular location but also given the hot mirror, quantum efficiencies of the photomultipliers and the cutoff filter installed in front of the R2228s (for details see Chapter 3). The signal for the VIS PMTs (R6095) quickly drops to zero for $\theta_{min} > 10.0$ mrad, thus they are useful only for detecting and discriminating the plentiful synchrotron backgrounds. It is also evident from looking at the tables how sensitive the signal is to changes in σ_z – an increase of less than 6% in σ_z results in a 40-50% decrease in signal.

5.4 Interpreting the Tables

5.4.1 CESR Currents and Scaling the Rates

CESR currents are typically asymmetric (for example, a positron current of 70 mA with an electron current of 60 mA), and decrease by about 15% before being topped up by additional injections. They also vary somewhat from run to run. Here we have chosen to standardize both currents at 55 mA, a typical value, with the idea that rescaling can be easily done as needed. Rates for other currents can be obtained by multiplying the rates by $I_+^2 I_-/(55^3)$, for the e^- beam, and $I_+ I_-^2/(55^3)$ for the e^+ beam (currents in mA). Rescaling is also necessary when there is a change in the number of bunches.

Energy (GeV)	2.1	1.89
Bunch Currents, I_-, I_+(mA)	55	55
No. of Bunches	24	24
σ_x (microns)	367	403
σ_y (microns)	7	7
σ_z (mm)	10.7	11.3

Table 5.1: Summary of CESR Parameters used for the expected rates calculations, HEP conditions, 2006-2007.

5.4.2 Beam Crossing Angle

CESR electron and positron beams are made to collide with a "crossing angle" θ_{cross} in the horizontal (x-z) plane. This angle, actually a half-angle, is on the order of a few milliradians and varies with the lattice. The crossing angle effectively increases θ_{obs}, the observation angle, thus the signal in the VIS and NIR regime becomes correspondingly weaker with increasing θ_{cross}. For an on-axis collision with zero-crossing angle (essentially a head-on collision), the observation angle from the beam's centroid to our detector is approximately 9.27 mrad. Applying Equation 4.11 to the CLEO Timelines data presented in Chapter 4, we computed the following effective observation angles. Included for comparison are the value

computed for the typical crossing angle from the CESR Phase III era [4] as well as the value for the on-axis/zero-crossing angle case.

Date	θ_{cross} (mrad)	θ_{obs} (mrad)
On-axis	0.00	9.27
1990s	2.00	10.05
Aug 2006	2.96	10.54
Sep 2006	2.925	10.53
Jul/Aug 2007	3.071	10.61

Table 5.2: Beamstrahlung detector observation angle θ_{obs} calculated for different values of beam crossing angle θ_{cross}

Table 5.2 gives an indication of which lines to look at in the following Tables of Expected Rates in order to determine reasonable expected signal rates given a set of CESR conditions including the crossing angle. Essentially the θ_{obs} are the relevant θ_{min} values.

5.5 Tables of Expected Large Angle Beamstrahlung Detection Rates

The first 8 tables are for an energy of 2.1 GeV per beam, and the following 8 are for 1.89 GeV per beam.

Rate for:	R6095(VIS)		R316-02(NIR)		R2228(NIR)	
θ_{min} mrad		w/CAD		w/CAD		w/CAD
9.0	1707	4455	4522	5410	18916	25392
9.2	869	2655	3252	4064	12675	18137
9.4	432	1505	2312	2986	8350	12593
9.6	210	820	1623	2156	5406	8548
9.8	99	432	1125	1532	3439	5690
10.0	45	222	770	1070	2149	3713
10.2	20	111	498	730	1276	2370
10.4	8	55	293	484	696	1471
10.6	3	26	154	308	341	881
10.8	2	12	61	186	127	505
11.0	0	6	27	106	55	273
CESR parameters: Energy			2.1 GeV			
Bunch Currents (I_+, I_-)			55,55 mA			
σ_x, σ_y, σ_z			367 μm, 7 μm, 10.7 mm			
No. of Bunches			24			

Table 5.3: Expected large angle beamstrahlung signal detection rates at CESR, 2006-2007, varying parameters: 2.1 GeV,σ_x=367 μm, σ_z= 10.7 mm

	R6095(VIS)		R316-02(NIR)		R2228(NIR)	
θ_{min} mrad		w/CAD		w/CAD		w/CAD
9.0	622	1944	2524	3369	9519	14487
9.2	309	1100	1784	2452	6235	9966
9.4	150	598	1243	1752	4010	6704
9.6	71	315	846	1229	2517	4417
9.8	33	162	556	844	1529	2848
10.0	14	81	346	565	883	1791
10.2	6	40	193	366	463	1093
10.4	2	19	95	227	215	643
10.6	0	9	38	134	83	362
10.8	0	4	10	75	20	193
11.0	0	2	3	39	6	97
CESR parameters: Energy			2.1 GeV			
Bunch Currents (I_+, I_-)			55,55 mA			
σ_x, σ_y, σ_z			367 μm, 7 μm, 10.7 mm			
No. of Bunches			24			

Table 5.4: Expected large angle beamstrahlung signal detection rates at CESR, 2006-2007: varying parameters: 2.1 GeV,σ_x=367 μm, σ_z= 10.7 mm, triangular acceptance

Rate for:	R6095(VIS)		R316-02(NIR)		R2228(NIR)	
θ_{min} mrad		w/CAD		w/CAD		w/CAD
9.0	778	2335	3198	3990	12212	17478
9.2	377	1356	2243	2941	7913	12192
9.4	178	745	1553	2116	5034	8246
9.6	82	392	1061	1494	3143	5441
9.8	36	199	715	1037	1925	3516
10.0	16	98	475	707	1156	2225
10.2	7	47	299	472	662	1378
10.4	3	22	172	306	349	830
10.6	1	10	88	191	166	484
10.8	0	5	34	114	59	270
11.0	0	2	15	64	25	143
CESR parameters: Energy			2.1 GeV			
Bunch Currents (I_+, I_-)			55,55 mA			
σ_x, σ_y, σ_z			367 μm, 7 μm, 11.3 mm			
No. of Bunches			24			

Table 5.5: Expected large angle beamstrahlung signal detection rates at CESR: 2006-2007, varying parameters: 2.1 GeV,σ_x=367 μm, σ_z= 11.3 mm

Rate for:	R6095(VIS)		R316-02(NIR)		R2228(NIR)	
θ_{min} mrad		w/CAD		w/CAD		w/CAD
9.0	270	984	1720	2404	5873	9594
9.2	128	540	1184	1714	3716	6432
9.4	59	284	803	1198	2306	4210
9.6	26	144	532	822	1397	2696
9.8	11	71	341	553	819	1689
10.0	5	34	207	362	457	1033
10.2	2	16	113	230	233	614
10.4	0	7	55	141	106	352
10.6	0	3	22	82	40	194
10.8	0	2	5	45	9	101
11.0	0	0	1	23	2	50
CESR parameters: Energy				2.1 GeV		
Bunch Currents (I_+, I_-)				55,55 mA		
σ_x, σ_y, σ_z				367 μm, 7 μm, 11.3 mm		
No. of Bunches				24		

Table 5.6: Expected large angle beamstrahlung signal detection rates at CESR: 2006-2007, varying parameters: 2.1 GeV,σ_x=367 μm, σ_z= 11.3 mm and triangular acceptance

Rate for:	R6095(VIS)		R316-02(NIR)		R2228(NIR)	
$\theta_{min} mrad$		w/CAD		w/CAD		w/CAD
9.0	648	1944	2662	3322	10165	14548
9.2	314	1128	1867	2448	6587	10149
9.4	148	620	1293	1761	4190	6863
9.6	68	326	883	1244	2616	4529
9.8	30	165	595	863	1602	2926
10.0	13	82	395	589	812	1852
10.2	6	39	249	393	551	1147
10.4	2	18	143	255	292	691
10.6	0	9	74	159	138	403
10.8	0	4	29	95	50	225
11.0	0	2	13	53	21	119
CESR parameters: Energy				2.1 GeV		
Bunch Currents (I_+, I_-)				55,55 mA		
σ_x, σ_y, σ_z				403 μm, 7 μm, 11.3 mm		
No. of Bunches				24		

Table 5.7: Expected large angle beamstrahlung signal detection rates at CESR: 2006-2007, varying parameters: 2.1 GeV,σ_x=403 μm, σ_z= 11.3 mm

Rate for:	R6095(VIS)		R316-02(NIR)		R2228(NIR)	
θ_{min} mrad		w/CAD		w/CAD		w/CAD
9.0	225	819	1432	2001	4889	7986
9.2	106	450	986	1426	3093	5354
9.4	49	237	669	998	1920	3504
9.6	22	120	443	685	1162	2244
9.8	10	59	284	460	682	1406
10.0	4	29	173	302	381	860
10.2	2	13	94	192	194	511
10.4	1	6	46	117	88	293
10.6	0	3	18	68	33	161
10.8	0	1	5	38	8	84
11.0	0	0	2	19	3	42
CESR parameters: Energy				2.1 GeV		
Bunch Currents (I_+, I_-)				55,55 mA		
σ_x, σ_y, σ_z				403 μm, 7 μm, 11.3 mm		
No. of Bunches				24		

Table 5.8: Expected large angle beamstrahlung signal detection rates at CESR: 2006-2007 varying parameters: 2.1 GeV,σ_x=403 μm, σ_z= 11.3 mm, triangular acceptance

Rate for:	R6095(VIS)		R316-02(NIR)		R2228(NIR)	
θ_{min} mrad		w/CAD		w/CAD		w/CAD
9.0	1421	3709	3764	4503	15745	21136
9.2	724	2211	2707	3383	10551	15097
9.4	360	1253	1924	2486	6902	10482
9.6	174	682	1352	1795	4501	7115
9.8	82	360	936	1275	2863	4736
10.0	38	185	641	890	1788	3092
10.2	17	93	414	608	1062	1972
10.4	7	45	244	403	580	1225
10.6	3	22	128	257	284	734
10.8	0	10	51	155	105	420
11.0	0	5	22	88	46	227
CESR parameters: Energy				2.1 GeV		
Bunch Currents (I_+, I_-)				55,55 mA		
σ_x, σ_y, σ_z				403 μm, 7 μm, 10.7 mm		
No. of Bunches				24		

Table 5.9: Expected large angle beamstrahlung signal detection rates at CESR: 2006-2007, varying parameters: 2.1 GeV,σ_x=403 μm, σ_z= 10.7 mm

Rate for:	R6095(VIS)		R316-02(NIR)		R2228(NIR)	
θ_{min} mrad		w/CAD		w/CAD		w/CAD
9.0	518	1618	2101	2804	7923	12059
9.2	268	915	1485	2041	5190	8296
9.4	125	498	1034	1458	3338	5581
9.6	59	263	704	1023	2095	3677
9.8	27	135	463	703	1273	2370
10.0	12	68	288	470	734	1491
10.2	5	33	161	304	385	910
10.4	2	16	79	189	179	536
10.6	0	7	32	112	69	301
10.8	0	3	8	62	17	161
11.0	0	2	1	33	5	81
CESR parameters: Energy				2.1 GeV		
Bunch Currents (I_+, I_-)				55,55 mA		
σ_x, σ_y, σ_z				403 μm, 7 μm, 10.7 mm		
No. of Bunches				24		

Table 5.10: Expected large angle beamstrahlung signal detection rates at CESR: 2006-2007, varying parameters: 2.1 GeV,σ_x=403 μm, σ_z= 10.7 mm and triangular acceptance

Rate for:	R6095(VIS)		R316-02(NIR)		R2228(NIR)	
θ_{min} mrad		w/CAD		w/CAD		w/CAD
9.0	1754	4579	4647	5560	19440	26095
9.2	893	2729	3342	4177	13026	18639
9.4	444	1547	2375	3069	8582	12941
9.6	215	842	1668	2216	5556	8785
9.8	102	444	1156	1574	3534	5847
10.0	47	228	791	1099	2208	3816
10.2	21	114	511	750	1311	2435
10.4	9	56	301	497	716	1512
10.6	3	27	158	317	350	906
10.8	1	12	63	192	130	518
11.0	0	6	28	109	56	280
CESR parameters: Energy				1.89 GeV		
Bunch Currents (I_+, I_-)				55,55 mA		
σ_x, σ_y, σ_z				403 μm, 7 μm, 10.7 mm		
No. of Bunches				24		

Table 5.11: Expected large angle beamstrahlung signal detection rates at CESR: 2006-2007, varying parameters: 1.89 GeV,σ_x=403 μm, σ_z= 10.7 mm

Rate for:	R6095(VIS)		R316-02(NIR)		R2228(NIR)	
θ_{min} mrad		w/CAD		w/CAD		w/CAD
9.0	639	1998	2598	3462	9782	14888
9.2	318	1130	1833	2520	6407	10242
9.4	154	615	1227	1800	4121	6890
9.6	73	324	869	1263	2587	4539
9.8	39	166	572	667	1571	2927
10.0	15	83	355	580	907	1841
10.2	6	41	198	376	475	1124
10.4	2	19	98	233	221	661
10.6	1	9	40	138	85	372
10.8	0	4	10	77	20	199
11.0	0	2	3	40	6	99
CESR parameters: Energy			1.89 GeV			
Bunch Currents (I_+, I_-)			55,55 mA			
σ_x, σ_y, σ_z			403 μm, 7 μm, 10.7 mm			
No. of Bunches			24			

Table 5.12: Expected large angle beamstrahlung signal detection rates at CESR: 2006-2007 varying parameters: 1.89 GeV,σ_x=403 μm, σ_z= 10.7 mm, triangular acceptance

Rate for:	R6095(VIS)		R316-02(NIR)		R2228(NIR)	
θ_{min} mrad		w/CAD		w/CAD		w/CAD
9.0	800	2400	3287	4101	12550	17962
9.2	387	1393	2305	3022	8132	12530
9.4	183	765	1596	2175	5173	8474
9.6	84	402	1090	1535	3230	5592
9.8	37	204	734	1066	1978	3613
10.0	16	101	488	727	1188	2287
10.2	7	48	307	485	680	1416
10.4	3	23	176	315	359	853
10.6	1	10	91	197	170	497
10.8	0	5	35	117	61	278
11.0	0	2	16	65	26	147
CESR parameters: Energy			1.89 GeV			
Bunch Currents (I_+, I_-)			55,55 mA			
σ_x, σ_y, σ_z			403 μm, 7 μm, 11.3 mm			
No. of Bunches			24			

Table 5.13: Expected large angle beamstrahlung signal detection rates at CESR: 2006-2007 varying parameters: 1.89 GeV,σ_x=403 μm, σ_z= 11.3 mm

Rate for:	R6095(VIS)		R316-02(NIR)		R2228(NIR)	
θ_{min} mrad		w/CAD		w/CAD		w/CAD
9.0	277	1011	1763	2470	6036	9859
9.2	131	555	1217	1761	3819	6610
9.4	60	292	825	1232	2370	4326
9.6	27	148	547	845	1435	2770
9.8	12	73	351	568	842	1736
10.0	5	35	213	372	470	1061
10.2	2	17	116	236	239	631
10.4	1	8	56	144	109	362
10.6	0	4	23	84	41	199
10.8	0	2	5	46	9	104
11.0	0	1	2	24	3	51
CESR parameters: Energy				1.89 GeV		
Bunch Currents (I_+, I_-)				55,55 mA		
σ_x, σ_y, σ_z				403 μm, 7 μm, 11.3 mm		
No. of Bunches				24		

Table 5.14: Expected large angle beamstrahlung signal detection rates at CESR: 2006-2007 varying parameters: 1.89 GeV,σ_x=403 μm, σ_z= 11.3 mm, triangular acceptance

Rate for:	R6095(VIS)		R316-02(NIR)		R2228(NIR)	
θ_{min} mrad		w/CAD		w/CAD		w/CAD
9.0	2107	5502	5583	6679	23354	31350
9.2	1073	3279	4016	5018	15649	22393
9.4	533	1859	2854	3687	10310	15547
9.6	259	1012	2003	2662	6675	10554
9.8	122	534	1389	1891	4246	7025
10.0	56	274	950	1320	2653	4584
10.2	25	137	614	901	1575	2826
10.4	11	67	361	597	860	1816
10.6	4	32	190	380	421	1088
10.8	0	15	75	230	155	623
11.0	0	7	34	130	68	337
CESR parameters: Energy				1.89 GeV		
Bunch Currents (I_+, I_-)				55,55 mA		
σ_x, σ_y, σ_z				367 μm, 7 μm, 10.7 mm		
No. of Bunches				24		

Table 5.15: Expected large angle beamstrahlung signal detection rates at CESR: 2006-2007, varying parameters: 1.89 GeV,σ_x=367 μm, σ_z= 10.7 mm

Rate for:	R6095(VIS)		R316-02(NIR)		R2228(NIR)	
θ_{min} mrad		w/CAD		w/CAD		w/CAD
9.0	768	2400	3116	4159	11752	17886
9.2	382	1358	2202	3027	7697	12305
9.4	185	739	1534	2163	4951	8278
9.6	88	389	1044	1517	3107	5454
9.8	40	200	687	1042	18538	3516
10.0	18	100	427	697	1090	2211
10.2	7	49	238	451	5071	1350
10.4	3	23	117	280	265	794
10.6	1	11	47	166	102	447
10.8	0	5	11	92	23	238
11.0	0	2	4	48	8	119
CESR parameters: Energy				1.89 GeV		
Bunch Currents (I_+, I_-)				55,55 mA		
σ_x, σ_y, σ_z				367 μm, 7 μm, 10.7 mm		
No. of Bunches				24		

Table 5.16: Expected large angle beamstrahlung signal detection rates at CESR: 2006-2007 varying parameters: 1.89 GeV,σ_x=367 μm, σ_z= 10.7 mm, triangular acceptance

Rate for:	R6095(VIS)		R316-02(NIR)		R2228(NIR)	
θ_{min} mrad		w/CAD		w/CAD		w/CAD
9.0	961	2883	3949	4927	15077	21579
9.2	465	1674	2770	3631	9770	15053
9.4	219	920	1917	2613	6215	10180
9.6	101	483	1310	1845	3880	6718
9.8	45	245	882	1281	2376	4340
10.0	20	121	586	873	1427	2748
10.2	8	58	369	583	817	1701
10.4	3	27	212	378	431	1025
10.6	1	13	109	236	205	598
10.8	0	6	42	140	79	334
11.0	0	3	19	78	32	176
CESR parameters: Energy				1.89 GeV		
Bunch Currents (I_+, I_-)				55,55 mA		
σ_x, σ_y, σ_z				367 μm, 7 μm, 11.3 mm		
No. of Bunches				24		

Table 5.17: Expected large angle beamstrahlung signal detection rates at CESR: 2006-2007, varying parameters: 1.89 GeV,σ_x=367 μm, σ_z= 11.3 mm

Rate for:	R6095(VIS)		R316-02(NIR)		R2228(NIR)	
θ_{min} mrad		w/CAD		w/CAD		w/CAD
9.0	333	1215	2124	2968	7251	11845
9.2	157	667	1462	2116	4588	7941
9.4	72	351	992	1479	2847	5198
9.6	32	178	657	1015	1724	3328
9.8	14	88	421	672	1011	2085
10.0	6	42	256	447	565	1275
10.2	2	20	140	284	287	758
10.4	1	9	67	173	130	435
10.6	0	4	27	101	49	239
10.8	0	2	7	56	12	125
11.0	0	1	2	29	4	62
CESR parameters: Energy			1.89 GeV			
Bunch Currents (I_+, I_-)			55,55 mA			
σ_x, σ_y, σ_z			367 μm, 7 μm, 11.3 mm			
No. of Bunches			24			

Table 5.18: Expected large angle beamstrahlung signal detection rates at CESR: 2006-2007, varying parameters: 1.89 GeV,σ_x=367 μm, σ_z= 11.3 mm and triangular acceptance

Chapter 6

Summary and Interpretation of Data

6.1 Introduction

Herein we present and discuss some data from the detector under analysis relevant to the search for a beamstrahlung signal. Included in the discussion is the data taking procedure and criteria for good data, fitting function, characterization of the dark rates of the PMTS, results of a typical scan used to point the detector, and the VIS signal rates, which are "pure" background, as can be seen from studying the tables given in Chapter 5 and the dark noise rate tables in this chapter.

6.2 Profile Scans and Identifying the Luminous Region

In the Profile Scan mode, the detector takes data at a grid of points potentially covering all possible slit positions. Effectively, this method scans the pointing angle of our device. The results of a Profile Scan may be used to identify the window sector containing the region receiving the most light from the IP so that the slits can be properly positioned during data taking. The horizontal and vertical slits are automatically moved across the window range by independently fixed increments. The detector records data at the rate of 1 record per position in the range. The resulting plots give a clear visual idea of the "luminous region"

where the light is coming from (see Figures 6.1 and 6.2). This information may then be useful in determining the horizontal and vertical coordinates of the slits for continuous data taking.

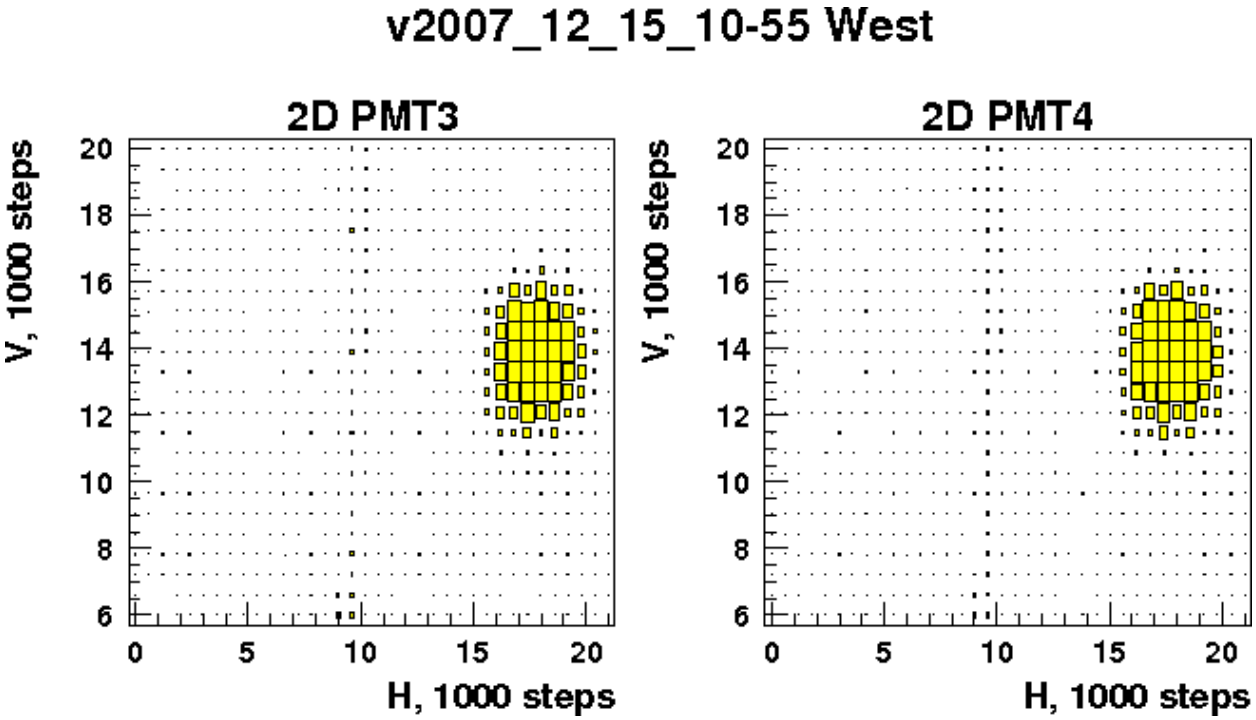

Figure 6.1: Two dimensional profile scan, West side 12/15/2007. PMT3 and PMT4 are the R6095 (VIS) x and y polarization components, respectively.

6.3 Data Taking Procedure

Our standard data taking procedure circa September 2007 is as follows:

1. Close the slits.

2. Take 600 records (about 12 minutes) with slits closed (dark noise data).

3. Set the slit coordinates so that a portion of the luminous region identified from a recent profile scan is in the center of the slits.

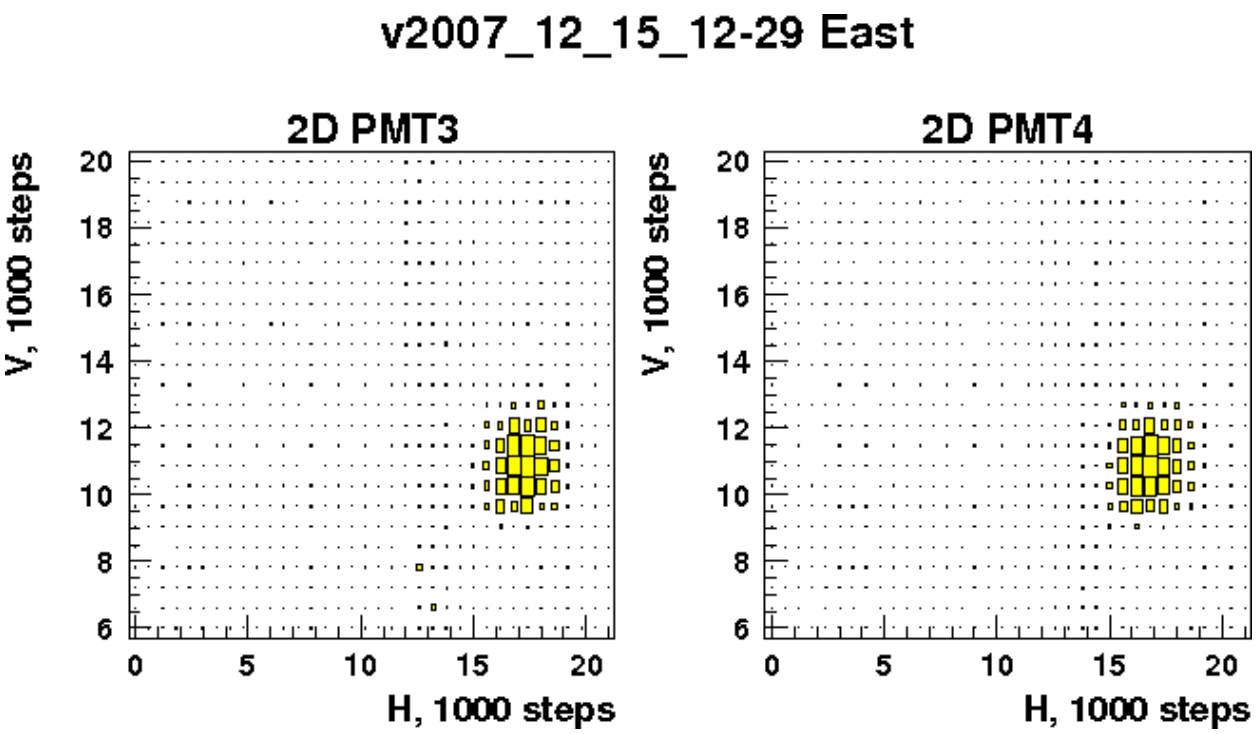

Figure 6.2: Two dimensional profile scan, East Side, 12/15/2007. PMT3 and PMT4 are the R6095 (VIS) y and x polarization components, respectively.

4. Take 20,000 records (about 8 hours) with slits open pointing toward the luminous region.

5. Close the slits.

6. Take 600 records with slits closed (dark noise data).

The criteria for good data are as follows:

- Decrease in beam currents is less than 2.7% on each 10 event interval.
- Increase in beam currents is less than 0.4% on each 10 event interval.
- Two luminosity parameters from the CESR dtabase, LUM and GLUM, remain within 20% of one another.

6.4 Data Analysis

The data are compacted by substituting every ten records with its average. The fitting function is:

$$R_i(t) = D_i + \beta_i I_{\pm}(t) + \alpha_i B_{\pm}(t) \tag{6.1}$$

where $R_i(t)$ is the data rate, D_i the dark noise (characterized in the next section), β_i is the parameter for the strength of the synchrotron backgrounds which vary linearly with the currents ($I_{\pm}$) and the subscript i refers to the ith PMT. Finally, α_i is the signal parameter, with the beamstrahlung radiator $B_{\pm}$ defined as follows:

$$B_{\pm} = K \frac{\Sigma_j I_{\pm j} I^2{}_{\mp j}}{f^3} \tag{6.2}$$

where K is a constant including the effects of such quantities as beam dimensions, emittance, and the detector observation angle, f is the revolution frequency, and the sum is over j circulating bunches.

6.5 Dark Rate

Based on statistical analysis of the dark rates it was determined that they are usually stable enough that the average of the dark rates at the beginning and the end of the run may be subtracted from the total rate as part of the preliminary signal search. Tables 6.1 and 6.2 present a comparison of average dark noise data from two runs separated in time by about 9 hours, as is typical based on our data-taking procedure. The runs which are presented here passed muster as "good" dark data, in the sense that the data meet the following criteria:

- A high percentage of the points are within 4 sigma of the mean.
- The ratio of the electronic channels monitoring the same PMT at the 1 Hz and 0.1 Hz rate is close to the expected value of 10.

- Calculated RMS close to the theoretical error.

Date	Start time	PMT1	PMT2	PMT9	PMT10
10/07/2007	12:18AM	525.91± 0.99	554.03± 0.98	854.04± 1.29	252.49± 0.79
10/07/2007	9:29AM	522.66± 0.93	553.79± 0.94	853.70± 1.30	251.07± 0.78

Table 6.1: A comparison of dark rates for the NIR PMTs before and after a typical 8 hour data taking period. Note that the rates remain quite stable, with typical errors less than 3 Hz.

Date	Start time	PMT7	PMT8	PMT15	PMT16
10/07/2007	12:18AM	5.36± 0.11	5.54± 0.11	7.34± 0.13	8.84± 0.14
10/07/2007	9:29AM	5.16± 0.10	5.44± 0.11	7.30± 0.12	8.92± 0.14

Table 6.2: A comparison of dark rates for the VIS PMTs before and after a typical 8 hour data taking period. Note that the rates remain stable, with an error of order 0.1 Hz.

For the NIR PMTS, the dark data error, on the level of a couple of Hz, and with rates of hundreds of Hz, one can conclude that the systematic error contributed is negligible. As for the VIS PMTs, the error is on the order of 0.1 Hz. Since the typical VIS signal rates are of order 10 kHz, the systematic errors for the VIS PMTs are also negligible. Therefore, we set the dark noise for each PMT equal to the average of the values before and after the run. This effectively eliminates a free parameter from our fitting function.

6.6 Synchrotron Radiation Backgrounds and Efficiencies

It is important to our effort to be able to properly characterize the synchrotron backgrounds perceived by our detector. The raw visible signal and the visible backgrounds are essentially one and the same, since both the dark noise systematic error and the beamstrahlung signal are negligible compared to these backgrounds. In terms of the fit function, we have α_i=0 and $\beta_i = 0$ for the VIS PMTS.

Date and Start Time	Fill Range (Record nos.)	PMT7 counts/mA-s	PMT8 counts/mA-s	PMT15 counts/mA-s	PMT16 counts/mA-s
10/07/2007 12:57AM	2100-2800	490	440	560	1600
10/07/2007 12:57AM	3500-4500	490	445	560	1600

Table 6.3: Visible PMT signal rates per milliamp for two fills during an 8 hour data taking run.

Table 6.3 displays some recent results for the signal from the visible PMTS. As expected, the backgrounds as a function of current are quite flat and very stable from fill to fill (see Fig. 6.3).

6.7 Flashlight Calibration

A calculation of the expected ratio of efficiencies for the detection of a flat synchrotron spectrum of the PMTs VIS:NIR ≈ 0.01. Analysis of the data showed that the measured detector efficiency was on the order of 0.001, an order of magnitude too low. The detector had to be re-calibrated. Calibration by means of a known broad spectrum light source (tungsten filament incandescent bulb) confirmed what we suspected – the efficiency of the NIR PMTs was indeed too low by an order of magnitude, suppressing the signal by an unacceptable amount. It appears that in our attempt to suppress the level of dark noise by decreasing the voltage level supplied to the PMTs, the efficiency was also suppressed. It is hoped that increasing the voltage will remedy this efficiency suppression and that we will still be able to deal with the resulting higher levels of dark noise by subtraction. However, the increase in dark rate could be so large that it will have a negative impact on the signal search. In that case it is we may have to revert to the use of the R316-02 PMTs with cooling, which will yield a somewhat smaller signal (see tables in Chapter 5), but with cooling, a reasonable level of dark noise.

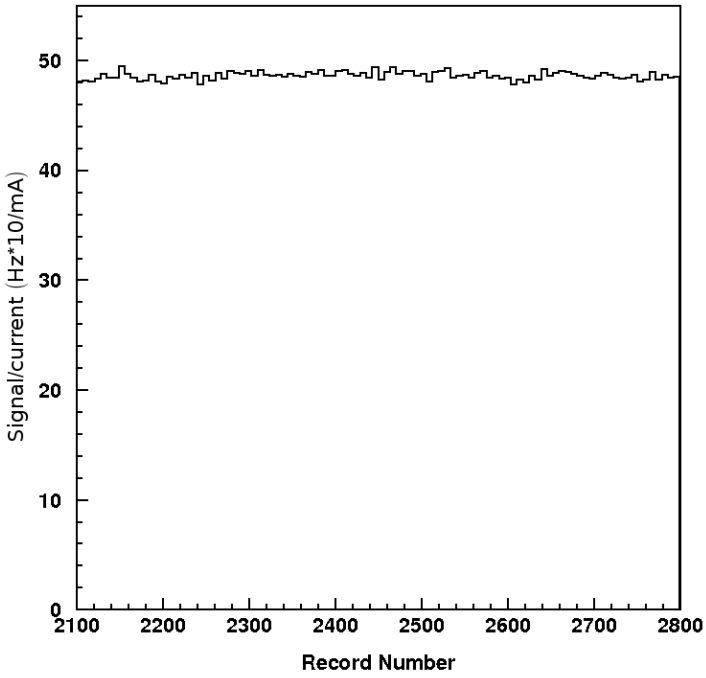

Figure 6.3: PMT7 signal to positron current ratio vs. record number for the first fill in Table 6.3 consisting of 700 records. This illustrates the expected flat synchrotron backgrounds observed via the VIS PMTs.

6.8 Future Work

Based on the expected signal tables, the signal for on-axis (pretzel off) single-bunch beams should be quite robust. As shown in Table 5.2, the observation angle is about 9.3 mrad, and from scrutiny of the signal tables in Chapter 4 we see that we may expect the NIR signal to be of order kHz. This strongly suggests that we might benefit from running an experiment of this type. In order to prepare for such an experiment we must first model the backgrounds for the on-axis orbit.

Bibliography

[1] R. Hollebeek, Nucl. Inst. and Meth. **184**, 333 (1981).

[2] N. Detgen et al., Preliminary Design of a Large Angle Beamstrahlung Detector at CESR, Technical Report CBN 99-26, Laboratory for Elementary Particle Physics, Cornell University, Ithaca NY 14853, 1999.

[3] J. A. Crittenden, Operational Status of CESR-c, Technical Report CBN 06-4, Laboratory for Elementary Particle Physics, Cornell University, Ithaca, NY 14853, 2006.

[4] R. M. Barnett et al., Phys. Rev. D **54**, 130 (1996).

[5] W.-M. Yao et al., Journal of Physics G **33**, 1+ (2006).

[6] A. Temnykh, Proceedings of PAC2005 , 189 (2005).

[7] A. W. Chao and M. Tigner, *Handbook of Accelerator Physics and Engineering, Chapter 4*, pages 277–281, World Scientific, Singapore, 2006.

[8] M. A. Furman, The Møller Luminosity Factor, Technical Report LBNL-53553, Lawrence Berkeley National Laboratory, Berkeley, California, 2003.

[9] M. Sands, The physics of electron storage rings: an introduction, Technical Report SLAC-0121, Stanford Linear Accelerator Center, Menlo Park, California 94025, 1970.

[10] S. Y. Lee, *Accelerator Physics*, World Scientific, Singapore, 2004.

[11] D. Sagan, S. Henderson, and J. Sikora, A Luminosity Monitor Using the Coherent Beam-Beam Interaction (Internal Report), Technical Report CBN 97-13, Laboratory for Elementary Particle Physics, Cornell University, Ithaca NY 14853, 1997.

[12] G. Bonvicini, D. Cinabro, and E. Luckwald, Phys. Rev. E **59**, 4584 (1999).

[13] G. Bonvicini et al., Phys. Rev. Let. **62**, 2381 (1989).

[14] J. D. Jackson, *Classical Electrodynamics, Chapter 14*, pages 661–698, Wiley, New York, 1999.

[15] R. Coïsson, Phys. Rev. A **20**, 524 (1979).

[16] M. Bassetti et al., IEEE Transactions of Nuclear Science **30**, 2182 (1983).

[17] G. Bonvicini and J. Welch, Nucl. Instr. and Meth. A **418**, 223 (1998).

[18] G. Bonvicini, Approximations for Large Angle Synchrotron Radiation, Technical Report CBN 98-12, Laboratory for Elementary Particle Physics, Cornell University, Ithaca NY 14853, 1998.

[19] M. E. Watkins and R. A. Briere, EventVertexProd and BeamSpotProc for CLEOIII, Technical Report CBX 03-31, Laboratory for Elementary Particle Physics, Cornell University, Ithaca, NY 14853, 2003.

ABSTRACT

LARGE ANGLE BEAMSTRAHLUNG DETECTOR FOR LUMINOSITY MONITORING AND OPTIMIZATION AT CESR

by

ERIC E. WISNIEWSKI

May 2008

Advisor: Professor Giovanni Bonvicini

Major: Physics

Degree: Master of Science

In electron-positron colliders, precision monitoring of beam-beam relative position, size, and orientation is essential to achieving and maintaining high luminosity. The case has been made for using large angle beamstrahlung detection as an effective means to more closely monitor the many degrees of freedom of the beam-beam collision at current and future colliders. Beamstrahlung is produced at every bunch crossing when charged particles in one beam are deflected by the electromagnetic field of the second, causing them to emit 'short magnet' synchrotron radiation. Beamstrahlung light is distinct from the more plentiful synchrotron light produced as the beam is bent by the dipoles and quadrupoles in the interaction region. Important distinguishing characteristics include wider angular spread and broader spectrum. Despite the comparatively small amount of beamstrahlung power available, by carefully choosing both a large enough angle and a low enough frequency range to observe, the signal-to-noise ratio can be made favorable. Since the ratio of vertically polarized to horizontally polarized light (relative to the plane of the storage ring) for a given azimuthal location depends on beam-beam offset and other luminosity wasting pathologies, extracting the polarization information is critical to the operation. A prototype large angle beamstrahlung detector has been constructed at the Cornell Electron Storage Ring (CESR) and is now in operation. This thesis focusses on the investigation of the expected signal for the current CESR conditions, which are quite different from when the detector was initially

proposed. The model incorporates the physics of beamstrahlung, detector optics, and PMT quantum efficiencies. Important parameters required for the model were calculated using measurements obtained from the CESR and CLEO timelines databases. The detector still requires some fine-tuning, but overall the prognosis looks good for detection of beamstrahlung at CESR in the near future.

Autobiographical Statement

Name: Eric E. Wisniewski

Education:

M.S. Physics, Wayne Sate University, Detroit, MI, 2008

Michigan Secondary Teaching Certificate, Michigan State University, East Lansing, MI 1987

B.A. Physics, Carleton College, Northfield, Minnesota, 1986

Professional Experience:

Graduate Research Assistant, Dept. of Physics and Astronomy, WSU, 2005-2008

Physics and AP Calculus teacher, Dearborn Public Schools , Dearborn, MI 1991-2005

Computer Science and Mathematics teacher, Cherry Hill High School, Westland, MI 1989-1991

Science and Mathematics teacher, Whitmore Lake High School, Whitmore Lake, MI, 1987 -1989

Publications:

Otto, N., Feng, J., Chen, R., Wisniewski, E. Linearity of Powertrain Acceleration Sound, SAE 971982.

Other Relevant Experience:

Prior to becoming a graduate student at Wayne State, I participated in two RET programs through Wayne State Physics Dept., working two summers in the LEPP at Cornell. The subject of my thesis is the detection and analysis of large angle beamstrahlung radiation at CESR. As a graduate research assistant I have gained extensive experience with various physics analysis and accelerator physics software including PAW, ABCI (wakefield simulation software) which I used to help evaluate the possibility of detecting coherent microwave beamstrahlung radiation at CESR, and CESRV (storage ring modeling software at CESR Cornell) which I have used extensively to acquire the parameters for different lattice configurations which we need for our synchrotron radiation backgrounds simulation software. In 2006 I

worked with my advisor G. Bonvicini on development of the software tools (FORTRAN) for analysis of large angle beamstrahlung in e-e+ colliders, including the background calculation program I already mentioned, and another program to calculate the expected beamstrahlung signal for our detector (which is installed at CESR), writing, revising and testing much code myself.